Mechanical behavior, failure mode, and transport properties in a porous carbonate

Patrick Baud, Ulrike Exner, Marco Lommatzsch, Thierry Reuschlé, Teng-Fong Wong

AGU PUBLICATIONS

JGR

Journal of Geophysical Research: Solid Earth

RESEARCH ARTICLE
10.1002/2017JB014060

Key Points:
- New triaxial experiments, petrophysical and CT data on Leitha limestone of porosity ranging from 18 to 31%
- Simple relation between porosity and strength over a wide range of pressures
- Compaction bands developed in less cemented samples of Leitha limestone

Supporting Information:
- Table S1
- Table S2

Correspondence to:
P. Baud,
patrick.baud@unistra.fr

Citation:
Baud, P., U. Exner, M. Lommatzsch, T. Reuschlé, and T.-f. Wong (2017), Mechanical behavior, failure mode, and transport properties in a porous carbonate, *J. Geophys. Res. Solid Earth*, *122*, 7363–7387, doi:10.1002/2017JB014060.

Received 2 FEB 2017
Accepted 8 AUG 2017
Accepted article online 12 AUG 2017
Published online 12 SEP 2017

Mechanical behavior, failure mode, and transport properties in a porous carbonate

Patrick Baud[1], Ulrike Exner[2], Marco Lommatzsch[3], Thierry Reuschlé[1], and Teng-fong Wong[4]

[1]Institut de Physique du Globe de Strasbourg, UMR 7516, CNRS, Université de Strasbourg/EOST, Strasbourg CEDEX, France, [2]Department of Geology and Palaeontology, Natural History Museum, Vienna, Austria, [3]Department of Geodynamics and Sedimentology, University of Vienna, Vienna, Austria, [4]Earth System Science Programme, Faculty of Science, The Chinese University of Hong Kong, Hong Kong

Abstract We performed a systematic investigation of mechanical compaction, strain localization, and permeability in Leitha limestone. This carbonate from the area of Vienna (Austria) occurs with a broad range of grain sizes and porosity, due to changes in depositional regime and degree of cementation. Our new mechanical data revealed a simple relation between porosity and mechanical strength in both the brittle and ductile regimes. Increasing cementation and decreasing porosity led to a significant increase of the rock strength in both regimes. Micromechanical modeling showed that the dominant micromechanisms of inelastic deformation in Leitha limestone are pore-emanated microcracking in the brittle regime, and grain crushing and cataclastic pore collapse in the ductile regime. Microstructural analysis and X-ray computed tomography revealed the development of compaction bands in some of the less cemented samples, while more cemented end-members failed by cataclastic flow in the compactant regime. In contrast to mechanical strength, permeability of Leitha limestone was not significantly impacted by increasing cementation and decreasing porosity. Our microstructural and tomography data showed that this was essentially due to the existence of a backbone of connected large macropores in all our samples, which also explained the relatively high permeability (in the range of 2–5 darcies) of Leitha limestone in comparison to other carbonates with significant proportion of micropores.

1. Introduction

The analysis of deformation and failure in many sedimentary successions hinges upon a fundamental understanding of the inelastic behavior and failure mode of porous rocks and their implications on fluid flow at various scales. For siliciclastic rocks such as sandstone, the processes leading to inelastic deformation and strain localization have been studied extensively in the past decades [*Aydin et al.*, 2006; *Wong and Baud*, 2012]. Experimental studies revealed in particular that the mechanical strength of these rocks is to the first order controlled by their porosity and grain size [*Zhang et al.*, 1990; *Wong et al.*, 1997; *Rutter and Glover*, 2012]. The main mechanisms of inelastic compaction in sandstone are grain crushing and pore collapse that can be either homogeneously distributed and leads macroscopically to cataclastic flow [*Wu et al.*, 2000] or localized in compaction bands [*Baud et al.*, 2004]. In both cases, significant permeability reduction is associated with inelastic compaction [*Zhu and Wong*, 1997; *Baud et al.*, 2012].

In porous carbonates, the phenomenology of brittle failure and inelastic compaction as reported by laboratory studies [*Vajdova et al.*, 2004; *Bemer et al.*, 2004; *Baud et al.*, 2009] is similar to that of sandstone over a wide range of porosities [*Wong and Baud*, 2012]. However, additional complexity specific to carbonates renders constitutive modeling of these rocks significantly more challenging than for sandstones. First, carbonate rocks are widely recognized to have pore geometry that is significantly more complex than other sedimentary rocks [*Choquette and Pray*, 1970; *Lucia*, 1995]. One of the reasons for the geometric complexity is that depositional environment and diagenesis exert significant genetic influence over the development of depositional texture and fabric of a carbonate rock [*Folk*, 1980; *Tucker and Wright*, 1991], which can in turn modify both the size and connectivity of the pore space in a relatively rapid and dramatic manner. The pore size in a carbonate rock may span over a very broad range, with a distribution that is often bimodal, including a significant subset of microporosity [*Pittman*, 1971; *Baechle et al.*, 2008; *Zhu et al.*, 2010]. Second, while stress-induced microcracking could be observed in laboratory deformed samples of carbonates over a wide range of conditions [*Baud et al.*, 2009; *Vajdova et al.*, 2010, 2012; *Brantut et al.*, 2014], crystal plasticity [*Turner et al.*, 1954; *Griggs et al.*,

1960; *Nicolas et al*., 2016] and pressure-solution [*Croizé et al*., 2013] can also potentially play an important role in these rocks even at modest temperatures. Field studies on carbonate formations [e.g., *Tondi et al*., 2006; *Tondi*, 2007; *Rath et al*., 2011] suggest that these mechanisms and others such as grain rotation, pore collapse, and grain crushing may lead to inelastic compaction and strain localization in carbonates. Additional complexity arises from the fact that these mechanisms are obviously influenced by microstructural parameters, such as the degree of cementation or the spatial distribution of macropores and micropores, but also by bedding heterogeneities. Possibly because of such complex situation, significant variability was observed in both the brittle strength [*Baud et al*., 2014] and the onset of inelastic compaction of carbonates, even for samples coming from the same sedimentary unit [*Dautriat et al*., 2011; *Cilona et al*., 2012; *Ji et al*., 2015].

A number of models have been proposed to capture the micromechanics of brittle and ductile failure in porous carbonate rocks. For brittle faulting, the pore-emanated crack model of *Sammis and Ashby* [1986] has proved to be in basic agreement with laboratory data on the strength as a function of porosity for a variety of limestones [*Zhu et al*., 2010; *Wong and Baud*, 2012; *Baud et al*., 2014]. In contrast, because the micromechanics of inelastic yield and failure in a carbonate rock are sensitive to the partitioning of macroporosity and microporosity, as well as their spatial distributions, there is not a single model that can capture the spectrum of ductile failure behavior. Several fundamentally different models have been proposed in the literature. A conventional pore collapse model [*Curran and Carroll*, 1979] whereby ductile failure develops from the plastic collapse of isolated pores may apply to a compact rock such as Solnhofen limestone [*Baud et al*., 2000]. However, this model is inadequate for many limestones which have comparable fractions of macroporosity and microporosity. To explicitly account for the distinct mechanical roles of the dual porosity in such rocks, *Zhu et al*. [2010] formulated a "cataclastic pore collapse model," which incorporates parameters that characterize the influence of micropore size and porosity partitioning on inelastic failure. They demonstrated that their model is in basic agreement with laboratory data for three micritric and allochemical limestones with porosities ranging from 10% to 31%.

In a recent study, *Regnet et al*. [2015] investigated porous carbonate rocks from the Oolithe Blanche Formation in France. The pore spaces of their samples are dominated by intercrystalline micropores related to micrites in ooids, whereas most preexisting macropores have been filled in by pervasive sparite cementation. Since their mechanical data were limited in scope, it was not possible to draw definitive conclusions regarding the failure mechanisms in this end-member with pervasive microporosity and negligible macroporosity. Nevertheless, this study has highlighted control of the spatial distribution of microporosity over the mechanical responses and failure modes. It also raises intriguing questions on the role of cementation and macroporosity in connection with failure in porous carbonate rocks, which we addressed in the present study.

We investigated systematically the mechanical behavior of a bioclast grainstone of Middle Miocene age (~12 Ma) from the Vienna Basin in Austria. [*Piller et al*., 2004]; the rock is generally referred to as Leitha limestone, which we will adopt for this paper. The limestone consists predominantly of one allochemical component (bioclasts) and interparticular macropores. These preexisting macropores have been coated with sparite calcite cement. Although there are micropores embedded in some of the bioclasts, they contribute relatively little to the total porosity, which varies significantly (18–31%) in the formation, primarily due to variable degree of cementation.

Thus, the Leitha limestone corresponds to the other end-member, with a pore space predominately made up of macropores. How do cementation and porosity influence the micromechanics of failure, and to what extent can it be described by models formulated for other carbonate rocks? The development of realistic micromechanical models requires not only mechanical data but also microstructural constraints. In this study, microstructure and inferred connection with cementation were investigated by cathodoluminescence (CL) and scanning electron microscopy (SEM), whereas the pore geometry and damage development were characterized quantitatively using X-ray computed tomography (CT).

A second objective of this study was to investigate the failure mode associated with brittle-ductile transition, and in particular, whether compaction bands may develop in the transitional regime. The development of compaction bands has been reported in several sandstone formations. Field [*Mollema and Antonellini*, 1996] and laboratory [*Cheung et al*., 2012] studies as well as numerical simulations [*Wang et al*., 2008] gave

consistent and rather precise insights on the microstructural attributes promoting the apparition of such failure mode. Under what conditions compaction bands can also develop in limestone is, however, still a matter of debate. While convincing field observations of compaction bands were presented in carbonate formations of the Majella mountain in Italy [*Tondi et al*., 2006; *Tondi*, 2007; *Rustichelli et al*., 2012], experimental studies gave so far contradictory results, suggesting that in limestone conditions for compaction band development might be somehow different than in sandstone [*Cilona et al*., 2012, 2014; *Ji et al*., 2015]. To our knowledge, compaction band formation has been observed in the laboratory only in a calcarenite [*Baxevanis et al*., 2006] and a chalk [*Tarokh et al*., 2016], but since neither study included microstructural observations pertinent to the pore geometry and damage development, very little is known regarding the microstructural attributes that may promote such a failure mode in highly porous carbonate rock.

Our final objective was to study the effect of porosity on hydraulic and electrical transport properties of Leitha limestone. Previous petrophysical data on carbonate rocks [*Lucia*, 1995; *Zinszner and Pellerin*, 2007; *Rashid et al*., 2015] have underscored a highly complex relation between hydraulic permeability, electrical conductivity, and porosity. For a given porosity, the permeability of carbonates can span over more than 3 orders of magnitude, probably related to the partitioning of porosity, size distribution of pores and throats, and their connectivity and spatial heterogeneity [*Tondi et al*., 2016; *Zambrano et al*., 2017]. To provide further microstructural constraints relevant to transport properties, mercury injection capillary pressure (MICP) measurements were conducted. Since we benefited from a rather unique set of samples that span over a broad range of porosity, the microstructure, and pore geometry of which have been systematically characterized, the new data would allow us to assess whether the dependence of transport properties on porosity agrees with predictions of preexisting models.

2. Geological Setting

At the margins of the Vienna Basin, Austria, Leitha limestone is exposed in numerous quarries. The Vienna Basin formed as a rhombohedral pull-apart basin at the junction between the Eastern Alps and the Western Carpathians during the Miocene [*Royden*, 1985; *Strauss et al*., 2006]. In the Middle Miocene (Badenian), the combination of eustatic sea level changes and fault activity led to a differentiation of depositional environments, where the central basin was filled with clastic material from the NW, providing the Matzen sandstone as one of the most productive onshore hydrocarbon reservoirs in Central and Western Europe [*Fuchs and Hamilton*, 2006]. Within the Matzen sands, repeated sea level changes also permitted the deposition of limestone horizons, which are regarded as similar to the Leitha limestone deposits at the basin margins. Some of these so-called *Nullipora* horizons (i.e., bioclastic grainstone beds) retained a relatively high porosity (11–21%), and due to lateral and vertical amalgamations with the sandstones, they also host hydrocarbons [*Kreutzer*, 1978]. At the same time, the Leitha platform represented a carbonate platform in the SE of the Vienna Basin, where thick Corallinacaena limestone beds accumulated; the platform was repeatedly subjected to sea level fluctuations and emersion [*Dullo*, 1983; *Schmid et al*., 2001]. Syndepositional to postdepositional tectonic activity along N-S trending normal faults resulted in a fragmentation of the Leitha platform, where middle Badenian mollusks and coral-rich, marly deposits dominate the western part of the platform, while the eastern part is covered only by late Badenian, more porous and Corallinacean-rich limestones [*Wiedl et al*., 2014]. *Rath et al*. [2011] described synsedimentary deformation bands in late Badenian carbonate grainstone at St. Margarethen/Burgenland, which are related to the exhumation of the Rust ridge and the subsidence of the Eisenstadt-Sopron basin along N-S trending normal faults.

The term Leitha limestone is stratigraphically somewhat imprecise, since it includes several lithologies comprising both middle and upper Badenian limestones, which show a great variability in content of bioclasts, carbonate mud and cements, terrigeneous material (detrital quartz, mica, and feldspar from the metamorphic hinterland and clay minerals), and porosity. These variations are also reflected in their petrophysical properties, as outlined by *Bednarik et al*. [2014], who sampled rocks from different quarries. All our samples come from the quarry "Hummel" [*Sauer et al*., 1992] at St. Margarethen/Burgenland (Figure 1a) and were selected from macroscopically pure carbonate material. Although the upper Badenian limestones are highly variable in porosity, grain size, and cementation between individual beds (Figures 1b and 1c), the types of bioclasts are relatively uniform in the rocks, comprising predominately corallinacean algae, bryozoans, foraminifers, bivalve and gastropod fragments, and echinoid debris [*Schmid et al*., 2001].

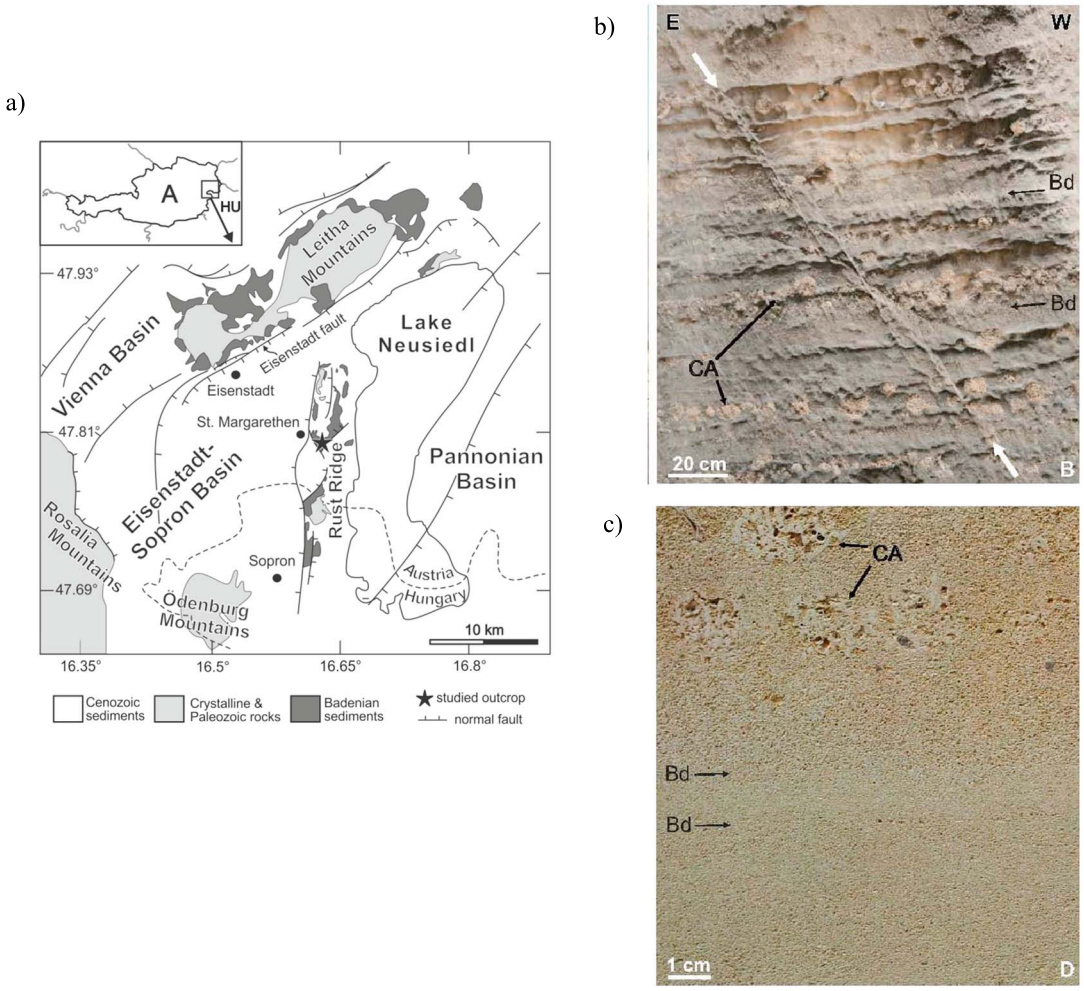

Figure 1. (a) Geological sketch map of the Eisenstadt-Sopron Basin in the SE of the Vienna Basin, Austria [modified after *Schmid et al*., 2001]. (b) Limestone outcrop in the quarry Hummel St. Margarethen/Burgenland. The white arrows indicate deformation bands; bedding (Bd) and Corallinacean algae (CA) are indicated. Note the variable weathering, indicating differences in porosity and cementation. (c) Typical yellowish, fresh cut slab of Leitha limestone perpendicular to bedding. Lamination/bedding is caused by variations in pore and grain size. Bedding (Bd) and red algae (CA) are indicated.

The diagenetic history of Leitha Limestone is described in detail by *Dullo* [1983], who investigated samples from the same quarry in St. Margarethen. Our own observations are in agreement with this previous work: The deposition of bioclasts in a shallow marine environment in the vicinity of small patchy reefs is associated by mass flows and subsequent incision and refilling of the seabed topography [*Schmid et al*., 2001]. This high-energy environment lead to a very high primary porosity (>30%) and is the reason for the lack of micritic carbonate matrix. Shallow-marine to phreatic conditions favored the generation of a blocky/sparry cement around the primary grain contacts, which preserved the primary high porosity and created a strong backbone of the rock fabric. Since sample location remained at a marginal position of the Eisenstadt-Sopron basin during further geodynamic evolution in the Miocene, it was not subjected to any major subsidence events or burial. Thus, no late diagenetic fluids or burial compaction affected the pore space and the cementation.

3. Experimental Methodology

3.1. Petrophysical Characterization and Transport Property Measurement

Fifteen blocks were gathered from the quarry Hummel, with the intention to cover a wide range of porosities. Macroscopically uniform blocks with no sign of deformation bands or bedding were selected. Cylindrical samples (20 mm in diameter and 40 mm in length) were cored orthogonal to the sedimentary bedding.

Measurements of porosity and transport properties were performed in the Rock Physics laboratory of École et Observatoire des Sciences de la Terre Strasbourg on samples from each block. The porosities were measured by water imbibition and triple weight technique, as well as by helium pycnometer. We selected the five most homogeneous blocks with average porosities 18, 21, 25, 27, and 31%. For each block, we then eliminated the samples with porosity ±1% of the average measured on the block. MICP were conducted at University of Aberdeen [*Haines et al*., 2015]. Pore throat statistics were inferred from MICP data of four samples (with porosities of 18, 21, 26, and 31%) acquired using a minimum pressure step of 3 MPa.

Hydraulic and electrical transport properties were measured at room temperature. Hydraulic permeability was measured using gas (argon or nitrogen) by the steady state flow technique at a confining pressure of 2 MPa. Appropriate Forcheimer corrections for "turbulent flow" were made, following the protocol described by *Heap et al*. [2014a]. A total of eight samples with porosities ranging from 21% to 31% were studied. Electrical conductivity was measured at a fixed frequency of 4 kHz on a sample saturated with solutions of increasing NaCl concentrations, corresponding to fluid conductivities between 0.04 and 2 S/m. The specifically designed device consists of a frame with two spring-loaded electrodes connected to a WTW LF2000-type conductivity meter [*Wei et al*., 2016]. The saturated sample was covered with an adhesive tape to prevent any loss of fluid and suppress electrical conduction along the exterior surface. To infer the formation factor from electrical conductivity, the model of *Waxman and Smits* [1968] for the coupling of bulk conduction and surface conduction was adopted. Four samples with porosities ranging from 21% to 31% were studied.

3.2. Mechanical Deformation

Samples were dried in vacuo at 40°C for a minimum of 48 h and then saturated with deionized water. Uniaxial and triaxial compression experiments were performed at room temperature in the Strasbourg laboratory, following protocols of *Heap et al*. [2014b] and *Baud et al*. [2009], respectively. Jacketed samples were deformed in uniaxial compression at a nominal strain rate of 10^{-5}/s. For triaxial experiments, confining pressure ranged from 5 to 120 MPa. A computer controlled stepping motor connected to a pressure transducer regulated the confining pressure with an accuracy of 0.05 MPa. The axial load was applied by a piston controlled by a second computer-controlled stepping motor. Axial displacement was measured outside the pressure vessel with a capacitive transducer with accuracy 0.2 μm mounted on the moving piston and servo-controlled at a fixed rate (corresponding taking into account the machine stiffness to a nominal strain rate of 10^{-5}/s). All experiments were performed under fully drained conditions at a fixed pore pressure of 5 MPa. The pore volume change was recorded by monitoring the displacement of the pore pressure generator with an angular encoder. The porosity change was calculated from the ratio of the pore volume change to the initial bulk volume of the sample. Volumetric strain also inferred in our setup from the calibrated confining pressure regulation gave almost identical values than porosity change, as previously shown by *Baud et al*. [2009].

3.3. Microstructural Analysis

Microstructural analysis was performed on three intact and nine deformed samples. X-ray CT data were first acquired on the whole volume of these samples at the Department of Anthropology of the University of Vienna, using a Viscom X8060 NDT X-ray μCT scanner. The pixel size was 20 μm. The cropped image stacks were binarized using Otsu thresholding in the software ImageJ. From these, slice-based porosity profiles were created across each sample, ignoring all clusters below three pixels in size (60 μm). To quantify connectivity of the pore space, we used a MATLAB® script developed by *Voorn et al*. [2013] that determines clusters of voxels which are touching via faces, edges, or corners (26-connected neighborhoods).

Samples were then saturated with epoxy, and polished petrographical thin sections (30 μm thickness) were prepared in the vertical direction on the whole sample length for SEM analysis at the Department of Lithospheric Research, University of Vienna. CL analysis was also performed on one thin section. Carbon-coated thin sections were investigated with a FEI Inspect S scanning electron microscope. Backscattered electron images were obtained at an accelerating voltage of 10–15 kV and a beam current of 10–50 pA. Standard petrographic and CL images were acquired with a Lumic HC5-LM microscope with an acceleration voltage set at 14 kV and a beam current of 5–7 mA.

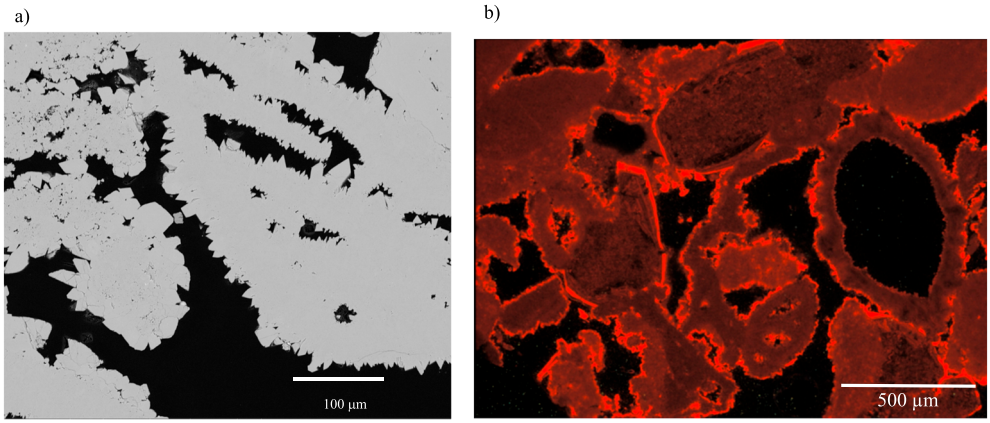

Figure 2. (a) Backscattered SEM micrograph of intact sample of Leitha limestone LM1 of 18% porosity showing microporous bioclasts coated by idiomorphic blocky cement without microporosity. (b) Cathodoluminescence image of Leitha limestone sample L0 of 32% porosity showing bioclasts coated by bright luminescent cement.

4. Microstructure and Petrophysical Properties

4.1. Petrophysical and Petrographical Characterization and Microstructure of Intact Leitha Limestone

Our samples can be categorized as carbonate grainstones composed of more than 99% calcite. Sampling within the available blocks from the quarry, we determined a broad range of porosities between 18 and 31%. A large majority of our samples had a nominal porosity of either 21 or 31%. Our study focused primarily on these two groups, as well as a few available samples from the low end-member of 18% porosity. Some measurements were performed on other samples of different porosities. We found that the porosity of a sample measured with water imbibition was less than that measured with pycnometer by on average 1%. We also note that porosity inferred from the bulk density of the samples (assuming 100% calcite of density 2.71 Mg/m^3) was always very close (less than 1% of difference) to the pycnometer measurements. This suggests the near absence of unconnected porosity in our samples, and we reported in Tables S1 and S2 in the supporting information the porosity of all samples used in this study inferred from the bulk density.

Our Leitha limestone samples are basically aggregates of cemented bioclasts (predominately corallinacean algae, bryozoans, foraminifers, bivalve and gastropod fragments, and echinoid debris). The bioclasts have a relatively homogeneous size. In samples of porosities 21% and 31%, we infer from SEM photomicrographs and quantitative image analysis the same average radius of 240 μm. Bioclasts in the most compact samples (porosity 18%) have a smaller average radius of 180 μm. The interstitial space is primarily made up by macropores (30–500 μm diameter), most of which are lined with a low-porosity, blocky sparry calcite cement [*Dullo*, 1983]. This early diagenetic product is manifested by a bright orange luminescence in the CL image. Even though the cementation may have sealed the grain contacts, most of the primary porosity is often conserved (Figures 2a and 2b).

We present in Figure 3 the μCT imaging data and SEM micrographs of three undeformed samples with porosities of 31% (Figures 3a–3d), 21% (Figures 3e–3h), and 18% (Figures 3i–3l), respectively. Spatial distribution of porosity imaged by μCT on individual slices seem homogeneous (Figures 3a, 3e, and 3i). For each slice, the areal porosity was evaluated, and the slices were then stacked to characterize the porosity as function of axial length (Figures 3b, 3f, and 3j). Overall the μCT data indicate that the spatial distribution of porosity is relatively homogeneous over the whole sample volume. The μCT data also indicate the pore space in each sample to be an interconnected network in 3-D. For each slice, the areal porosity that corresponds to this interconnected network was evaluated. It can be seen from the stacked data (Figures 3b and 3f) that the total and interconnected porosities basically coincide in the two most porous samples. Furthermore, difference between the total porosity and that resolved by μCT is relatively small, and since the latter is made up of macropores, the implication is that these samples have negligible microporosity. In contrast, consistent discrepancy of about 1% can be seen between the total and interconnected porosities in the most compact sample (Figure 3j), which suggests that isolated porosity exists in this case. Difference between the total porosity and that resolved by μCT is relatively large (~8%), which implies that this sample has significant microporosity.

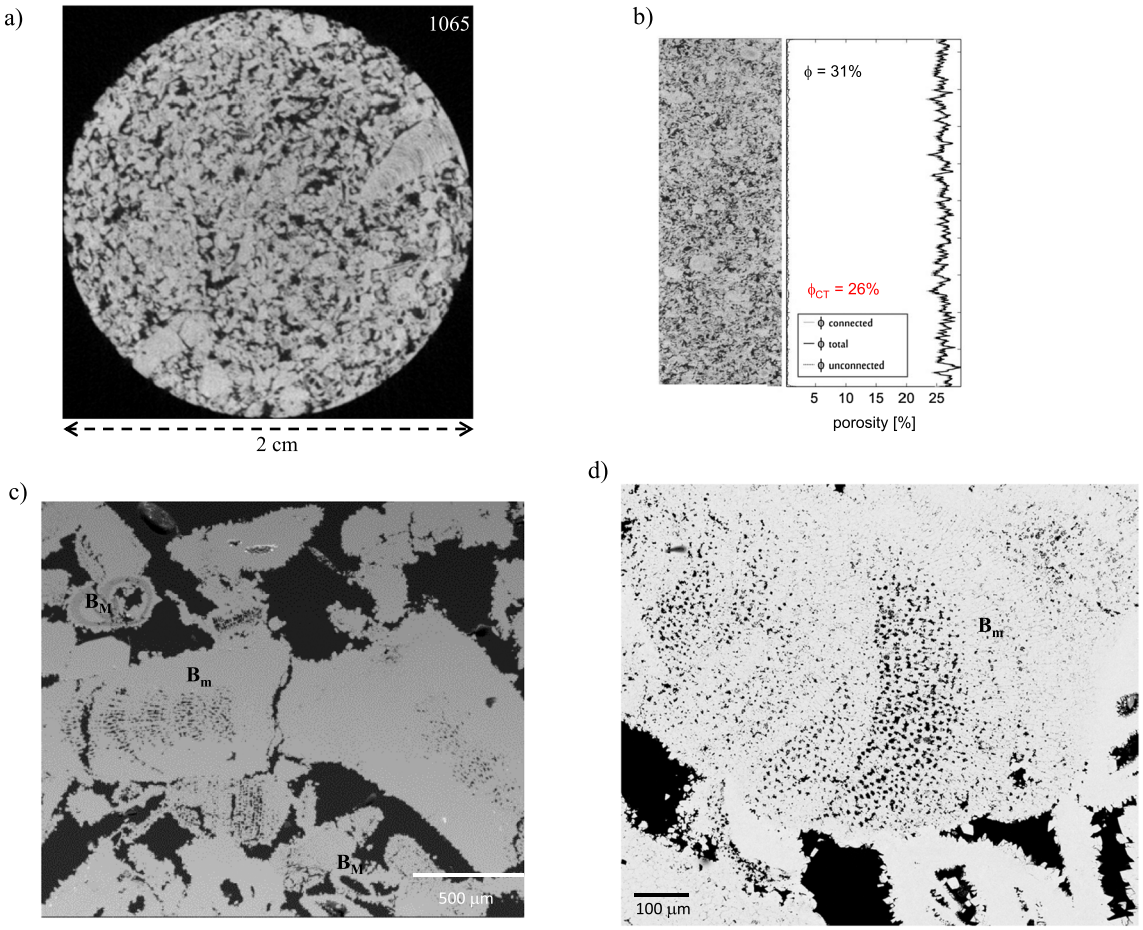

Figure 3. Microstructure of intact Leitha limestone of (a–d) 31%, (e–h) 21%, and (i–l) 18% porosity. μCT data with resolution 20 μm (Figures 3a, 3e, and 3i) showing a significant proportion of macropores (dark areas) in the intact rock. The slice number is indicated in the figures. Resliced μCT data (Figures 3b, 3f, and 3j) and statistics of total, connected, and unconnected porosity determined using the method presented by *Voorn et al.* [2013]. The porosity of samples inferred from the μCT images (total porosity) and measured using a pycnometer are given in black and red in the figures, respectively. The difference between these measures is the microporosity. Backscattered SEM images (Figures 3c and 3d, 3g and 3h, and 3k and 3l): Samples with 31% porosity (Figures 3c and 3d) contain bioclasts with high microporosity (5–10 μm pore diameter). Smaples with 21% porosity (Figures 3g and 3h) contain cemented bioclasts without or significantly less micropores. Samples with 18% porosity show smaller macropores (Figure 3k), smaller mean grain size, and thicker cement coatings, and bioclasts with high microporosity. Bioclasts with macroporosity (B_M) and with microporosity (B_m) are indicated in the images.

Under the SEM, some bioclasts (including bryozoans, foraminifers, and gastropods) were observed to have macropores (50–300 μm diameter) embedded in them (Figures 3c, 3g, and 3k). In contrast, corallinacean algae, which represent the largest and most abundant bioclasts, often have cellular growth rims embedded with micropores (5–10 μm diameter), which can readily be resolved under the SEM (Figures 3d and 3l), and are faintly discernible in μCT images (Figures 3a and 3i). We estimated from our μCT data that these intragranular macropores and micropores altogether contribute 7–9% toward the total porosity. It should be noted that in samples of 21% porosity, most corallinacean algae have been cemented by calcite (Figures 3h), thus retaining only up to 2% of intragranular porosity.

Morphological analysis was performed to extract pore size statistics from the interconnected network imaged by μCT using an ImageJ plugin (BoneJ), which determines the largest possible spheres inscribed in the pore space in 3-D across the image stack. Given their relatively large sizes, most of these should be categorized as macropores. The two samples with porosities of 31% (Figure 4a) and 21% (Figure 4b) have very similar distributions of macropore size, with mean values of 162 and 170 μm, respectively. The sample with 18% porosity (Figure 4c) has a higher proportion of small pores (60–120 μm diameter) and fewer pores larger than 150 μm diameter.

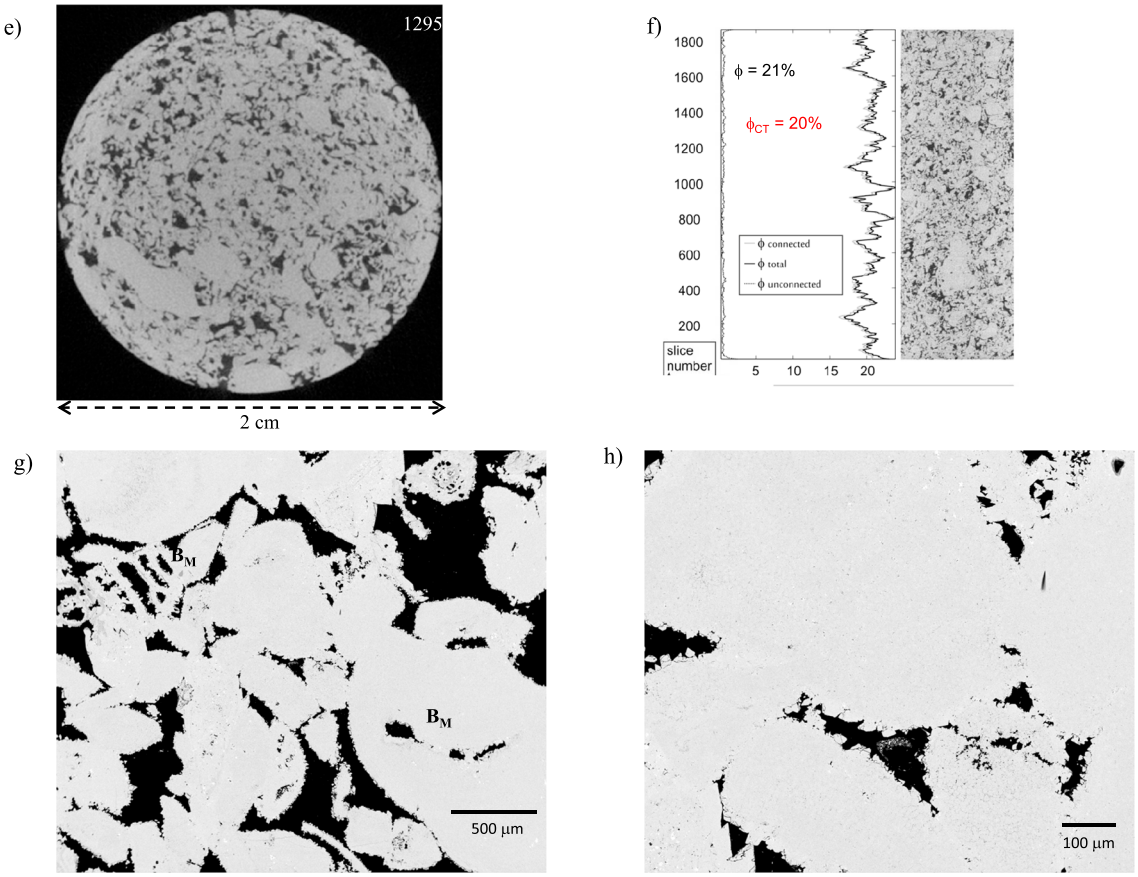

Figure 3. (continued)

Mercury injection capillary pressure analysis was used to infer the distribution of pore throat diameters in four samples (Figure 4d). Unlike a limestone with significant fractions of macroporosity and microporosity, which typically shows two inflection points in its MICP curve [*Zinszner and Pellerin*, 2007; *Zhu et al*., 2010; *Vincent et al*., 2011], our Leitha limestone samples consistently have only one inflection point in each curve. These inflection points correspond to pore throats with diameters >50 μm. The MICP data indicate that either the microporosity is insignificant (for the three more porous samples) or, even if there are many micropores (as in the 18% porosity sample), they are relatively small in dimension and contribute relatively little to hydraulic and electrical transport.

4.2. Transport Properties

There is an overall trend for permeability of Leitha limestone to increase with increasing porosity (Figure 5a). A moderate decrease from 8 to 2×10^{-12} m^2 was observed with porosity decreasing from 31% to 21%, followed by a dramatic decrease by at least 1 order of magnitude when porosity decreased further to 18%. We also investigated the pressure sensitivity of permeability in a sample with 21% porosity (Figure 5b). Under increasing confining pressure up to 20 MPa, permeability showed a minimal decrease from 2 to 1.8×10^{-12} m^2, with the implication that the Leitha limestone sample did not contain many microcracks, if any at all.

There is an overall trend for formation factor to increase with decreasing porosity (Table S1). A moderate increase from 15.4 to 25.2 was observed with porosity decreasing from 30% to 22%, followed by a dramatic increase by a factor of 3 when porosity decreased further to 18%.

5. Mechanical Data

In this paper we will use the convention that the compressive stresses and compactive strains (i.e., shortening and porosity decrease) are considered to be positive. We will denote the maximum and minimum

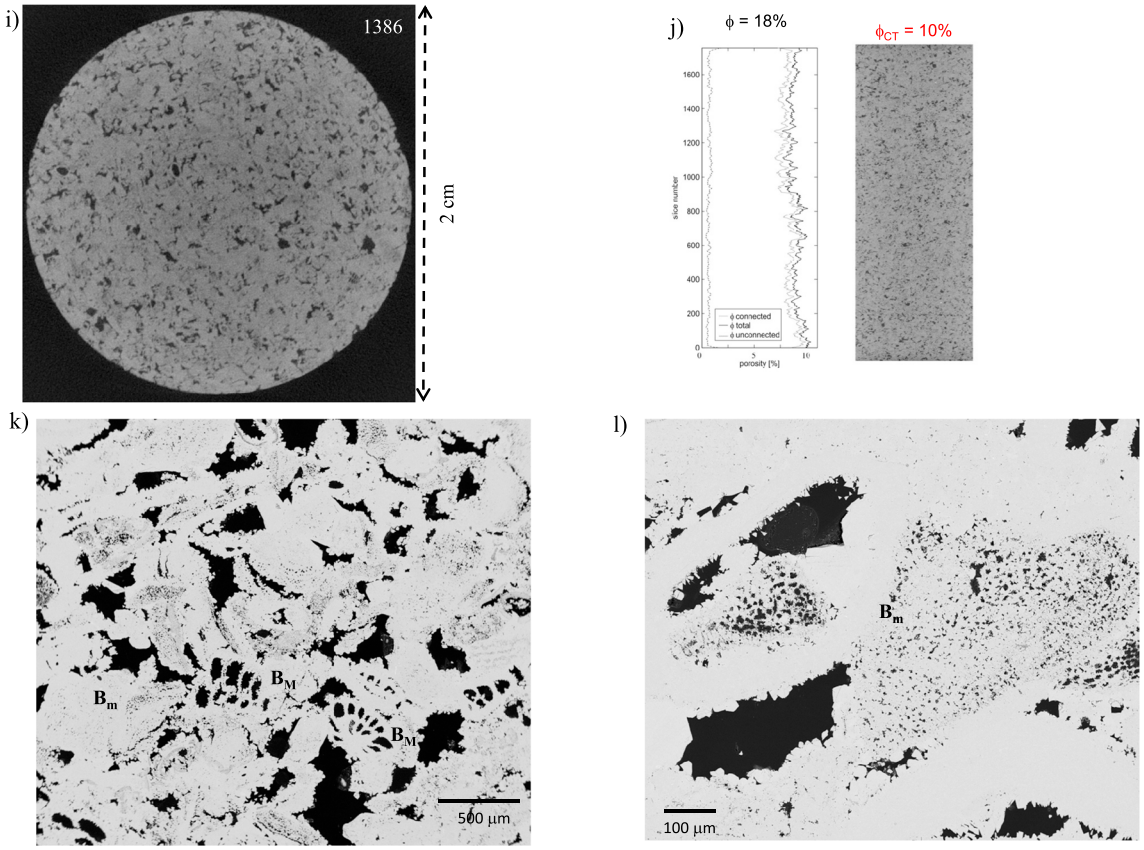

Figure 3. (continued)

(compressive) principal stresses by σ_1 and σ_3, respectively. The pore pressure will be denoted by P_p, and the difference $P_c - P_p$ between the confining pressure ($P_c = \sigma_2 = \sigma_3$) and pore pressure will be referred to as the "effective pressure" P_{eff}. The effective mean stress $(\sigma_1 + 2\sigma_3)/3 - P_p$ will be denoted by P and the differential stress $\sigma_1 - \sigma_3$ by Q.

Figure 6a presents our new uniaxial data on Leitha limestone. With decreasing porosity the uniaxial compressive strength (UCS) increased somehow regularly from 16 MPa to 50 MPa for a porosity decrease of 13%. As expected, the tangent modulus taken from the linear part of the stress-strain curves also increased by almost 50% for this porosity difference. All the samples presented in the Figure 6a failed by axial splitting.

Our hydrostatic data for the same porosity range are presented in Figure 6b. The observed behavior is qualitatively the same for the different porosities and also similar to what was previously reported for porous rocks [*Wong and Baud*, 2012]. The hydrostats could be separated in three successive stages: (1) The first nonlinear part at low effective pressures corresponds to microcrack closure. This part is not very pronounced at all in Leitha limestone, confirming the almost total absence of microcracks in this rock (Figure 5b). (2) Then the behavior becomes poroelastic (linear, reversible) and (3) beyond a critical pressure denoted P^* [*Wong et al.*, 1997], we observed an acceleration of the compaction corresponding to the onset of grain crushing and pore collapse. P^* can be therefore seen as the onset of inelastic compaction. Similar to the UCS, P^* increased quickly and regularly with decreasing porosity, from 28 MPa at 31% to 125 MPa at 18%. We noted, however, that if the compressibility of Leitha limestone decreased significantly when porosity decreased from 31% to 25% (from about a factor 3), it did not change between 25% and 21%, yet again decreased between 21% and 18%. Visual inspection of the samples deformed hydrostatically revealed in all cases a barrel shape typical of a failure by cataclastic flow.

Triaxial experiments were performed on the most abundant specimen types in terms of porosity (21 and 31%) in the effective pressure range 5–60 MPa. Representative data are presented in Figure 7. Figure 7a

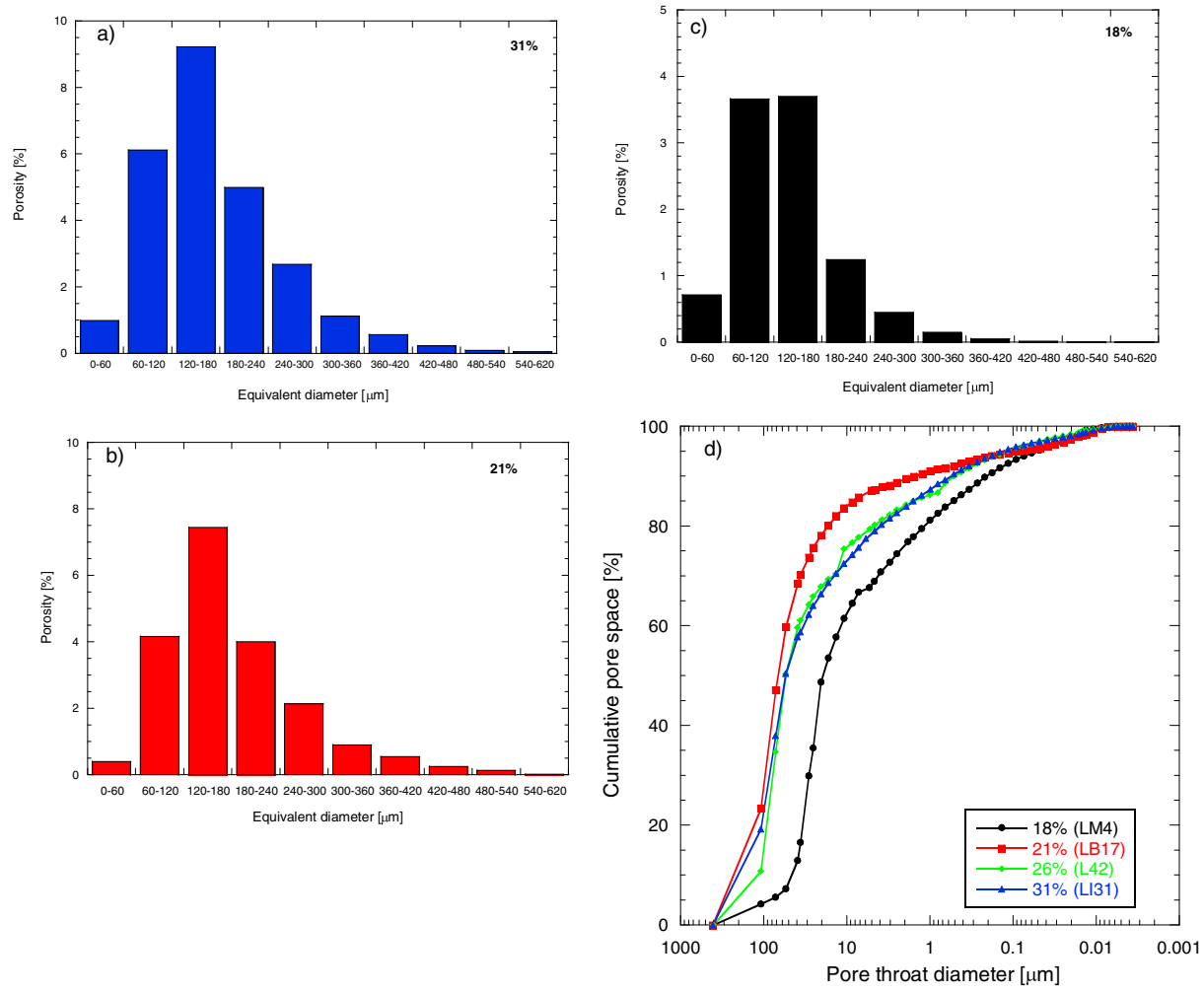

Figure 4. Distribution of macropore sizes inferred from μCT data for Leitha limestone of (a) 31%, (b) 21%, and (c) 18% initial porosity. (d) Cumulative pore space as a function of pore throat diameter inferred from mercury injection tests on intact samples of Leitha of 31% (blue), 26% (green), 21% (red), and 18% (black) initial porosity.

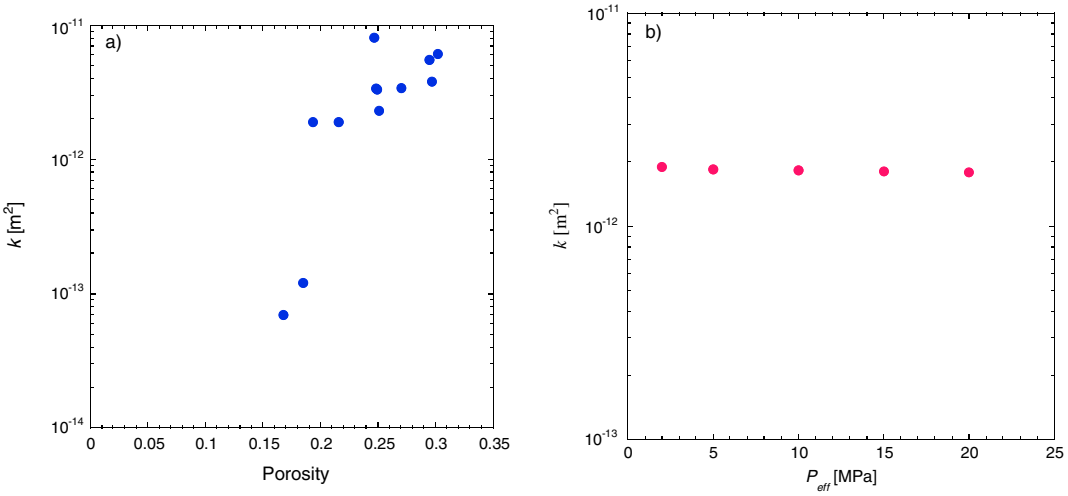

Figure 5. (a) Gas permeability as a function of porosity for a series of samples of Leitha limestone. (b) Gas permeability as a function of effective pressure for a sample of Leitha limestone of initial porosity 21%.

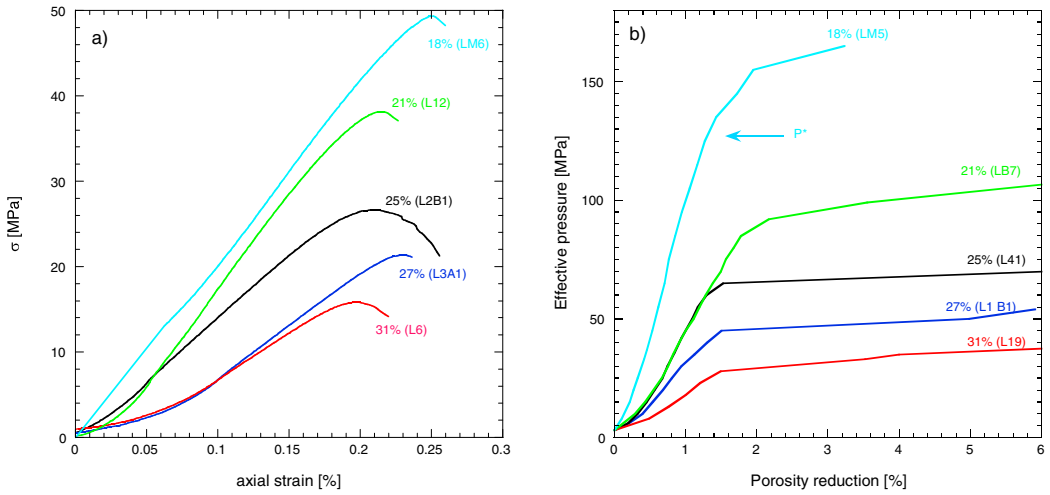

Figure 6. (a) UCS data on Leitha limestone. Axial stress is presented as a function of axial strain for uniaxial experiments performed on samples of different porosities. (b) Effective pressure as a function of porosity reduction in a hydrostatic experiments. The arrow indicates the critical pressure P^* for the onset of pore collapse. The initial porosity of the samples and the sample names (see Table S2) are indicated next to the curves.

shows a selection of stress-strain curves for the 31% porosity horizon. Even at the lowest tested pressure of 5 MPa, there was no clear indication of brittle behavior and the relatively flat stress-strain curve suggested more a transitional regime [*Baud et al.*, 2006]. With increasing effective pressure, we observed an increasing amount of strain hardening, typical of the ductile regime for porous materials. At all tested pressures the curves were punctuated by episodic stress drops, in some cases of high amplitude (up to 5 MPa). Previous studies showed that this is usually an indicator that some strain localization occurred in the samples [*Baud et al.*, 2004]. However visual inspection of the samples did not reveal any clear failure mode for samples of this block. We also observed a few stress drops in the data for the 21% porosity horizon (Figure 7c), but they were less pronounced. In this case, the data up to 10 MPa of effective pressure were typical of the brittle regime with a peak stress and strain softening. The samples showed clear shear bands at various orientations. Beyond P_{eff} = 10 MPa, ductile behavior was observed in all experiments, with again more significant strain hardening at higher effective pressures. Porosity change data are presented in Figures 7b and 7d. They are qualitatively the same for both blocks: no dilatancy was observed at any tested pressure, and all samples showed shear-enhanced compaction from critical stress noted C^*, the onset of inelastic compaction [*Wong et al.*, 1997]. At the highest tested pressures, we noted that for both blocks the porosity change versus axial strain curves have almost a slope of 1 beyond C^*, showing that inelastic compaction occurred with almost no radial strain.

Our triaxial and hydrostatic data are summarized in Figure 8 where the critical pressures P^* and C^* are presented in the stress space (differential stress as a function of effective mean stress). These data are also summarized in Table S2. For porosities of 21 and 31%, both triaxial data sets map out a single compactant yield envelope as it has been previously shown for other porous carbonates [*Baud et al.*, 2009]. Our triaxial data confirmed the large increase in strength induced by the cementation of Leitha limestone. Less abundant samples with intermediate (27 and 25%) and lower (18%) porosity were only tested in uniaxial and hydrostatic experiments, providing a frame for the expected yield envelopes.

6. Failure Mode and Damage Development

The uniaxially compressed samples all failed by axial splitting. For the triaxially compressed samples, we infer the failure modes (Figure 9) by visual inspection of the deformed samples, and in a few cases, by supplementary data from μCT imaging. The 21% porosity samples showed a transition of failure mode from brittle faulting to distributed cataclastic flow with increase in confinement. A single shear band was visible on the surface of the sample deformed at 10 MPa of effective pressure. Our mechanical data suggest that it should be categorized as a compactive shear band. In the transitional regime at 20 MPa effective pressure, conjugate shear bands developed on one extremity of the sample. Strain localization seems to be absent in the two samples

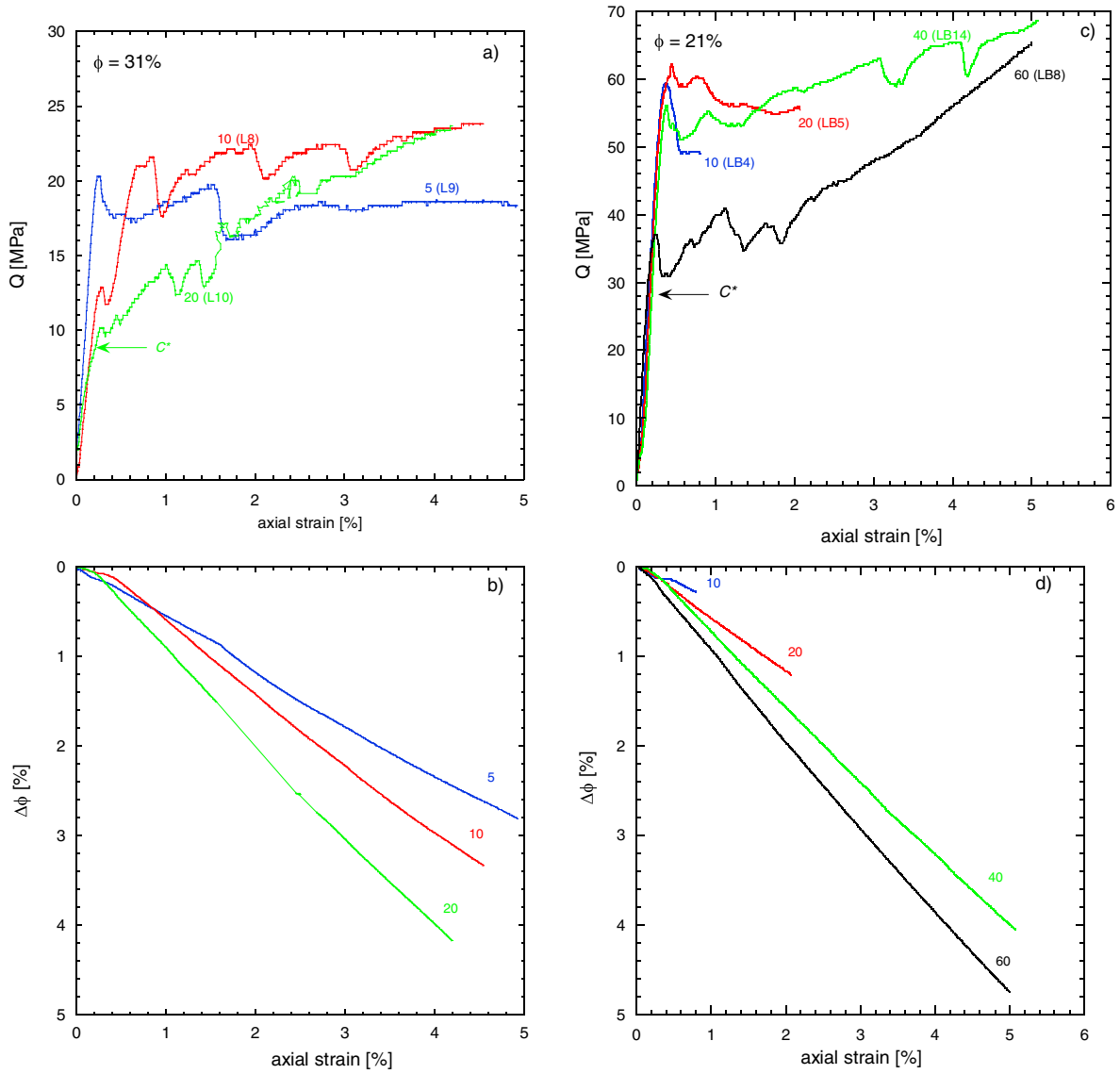

Figure 7. Mechanical data for triaxial compression experiments on Leitha limestone samples of initial porosity (a and b) 31% and (c and d) 21%. Differential stress as a function of axial strain (Figures 7a and 7c). Porosity reduction as a function of axial strain (Figures 7b and 7d). The effective pressures are indicated by the numbers next to each curve.

failed at effective pressures of 40 and 60 MPa. In contrast, brittle faulting was not observed in samples with 31% porosity that we deformed at effective pressures of 5 MPa and above. Whereas the ductile failure was all by cataclastic flow, the mode was localized at effective pressures of 5 and 10 MPa and distributed at 15 and 20 MPa.

The inferred failure modes are corroborated by the μCT data stacked to illustrate the axial distribution of porosity. In the 21% porosity sample that failed at an effective pressure of 20 MPa, development of the conjugate shear bands was manifested by significant reduction of porosity down to about 7% in a zone that spans from slice #200 to #400 (Figure 10a). Although it is beyond the scope of the present study to characterize the strain localization in 3-D, we expect the geometric complexity to be comparable to that recently observed in Majella limestone by digital correlation of μCT images [*Ji et al.*, 2015]. In the sample that failed at an effective pressure 60 MPa, porosity distribution is relatively homogeneous, with the implication that inelastic compaction was distributed (Figure 10b). Morphological analysis of the macropore size distributions in these two failed samples indicate that either failure mode was accompanied by an overall decrease of pore size, associated with the collapse of macropores with diameters bigger than 400 μm (Figure 10c). These data are in qualitative

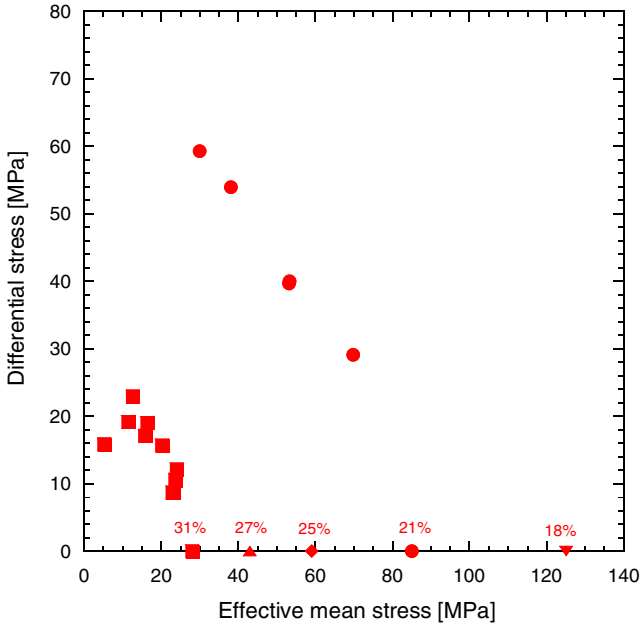

Figure 8. Compactive yield caps for onset of shear-enhanced compaction C^* in the effective mean stress and differential stress space for Leitha of 21% (red circles) and 31% (red squares) initial porosity. The onset of pore-collapse P^* is also shown for hydrostatic tests performed on intermediate (25 and 27%) and lower (18%) porosity samples.

agreement with the μCT imaging results of *Ji et al*. [2012] in their study of mechanical compaction of Indiana limestone.

In the 31% porosity sample that failed at effective pressure of 5 MPa, development of a diffuse compaction band is manifested by significant reduction of porosity down to about 20% in a zone that spans from slice #800 to #1050 (Figure 11a). At an effective pressure of 10 MPa, the compaction band spans from slice #200 to #500 (Figure 11b), with porosity reduction down to about 15%.

Our SEM observations elucidated the damage development associated with these failure modes in the samples with 21% porosity (Figure 12) and 31% porosity (Figure 13). In the former, axial splitting (at room pressure) and brittle faulting (at effective pressure of 10 MPa) were accompanied by propagation and linkage of pore-emanated cracks (Figure 12a) and development of an inclined shear band with localized cataclasis and fracturing of neighboring grains (Figure 12b), respectively. In the transitional regime at effective pressure of 20 MPa, development of the conjugate shear bands was accompanied by pervasive damage in the form of Hertzian fractures emanating from bioclast contacts, which would lead to grain crushing (Figure 12c) and pore collapse (Figure 12d). The progressive development of distributed cataclastic flow is illustrated by the damage observed in two samples deformed at an effective pressure 40 MPa to axial strains of 5% and 12%, respectively. Intragranular cracking, grain crushing, and pore collapse in the first sample (Figure 12e) seem not as intense and extensive as in the second (Figure 12f).

Compaction localization was observed in the samples with 31% porosity deformed under low confinement. Hertzian fractures emanating from bioclast contacts (Figure 13a) were pervasive in these samples. Intense grain crushing and pore collapse were evident inside the diffuse compaction bands in the samples deformed at 5 MPa (Figure 13b) and 10 MPa (Figures 13c and 13d), respectively. The progressive development of distributed cataclastic flow is illustrated by the damage observed in two samples deformed at effective pressure 20 MPa to axial strains of 4% (Figure 13e) and 14% (Figure 13f), respectively. In the latter, a relatively large bioclast (~1 mm in diameter) was almost completely crushed.

It should also be noted that mechanical twinning of cement overgrowth was observed in all deformed samples. From crosscutting relations, we infer that generally the twinning lamellae have developed prior to stress-induced microcracking. There seems to be an overall trend for twin density to increase with increasing effective pressure. However, because the twinning and microcracking tend to be intertwined, it is difficult to characterize quantitatively the twinning activity.

7. Discussion

7.1. Influence of Porosity on Brittle Strength of Leitha Limestone

The first objective of this study was to examine the influence of porosity on failure in Leitha limestone and the extent to which it can be described by micromechanical models formulated for other carbonate rocks. Our mechanical data show that indeed porosity exerts a first-order control on the mechanical

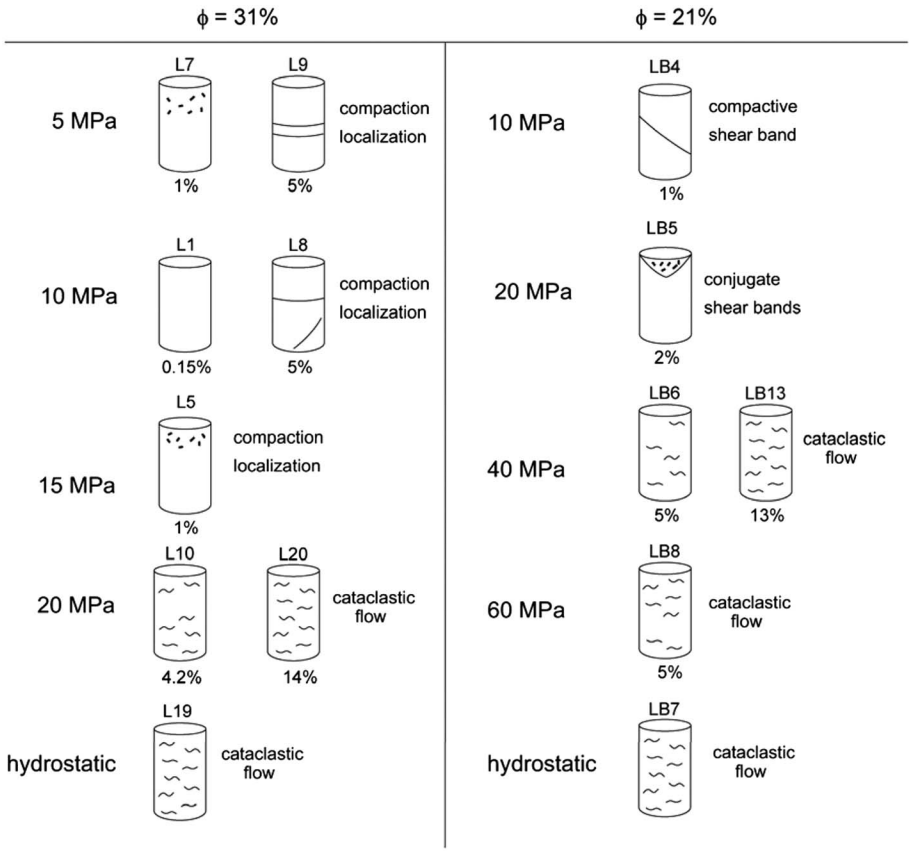

Figure 9. Cartoons summarizing the failure mode of Leitha limestone of initial porosity 21 and 31%, based on visual inspection and μCT data. Direction of σ_1 is vertical.

strength of Leitha limestone in both the brittle and ductile regimes. Under uniaxial compression, the UCS increases by more than a factor 3 when porosity decreases by 13%. This correlation between UCS and porosity can be fitted empirically by a quadratic relation (Figure 14a). It should be noted that such a systematic correlation was not observed in UCS data for a number of dry porous limestones that were compiled by *Baud et al.* [2014]. The likely reason is that additional microstructural attributes related to diagenesis and secondary porosity also have a significant influence on brittle failure in these other limestones.

Previous studies on porous limestones [e.g., *Vajdova et al.*, 2010, 2012] have indicated that the main micromechanism leading to brittle failure is the propagation and coalescence of pore-emanated microcracks, which can be captured by the damage mechanics model formulated by *Sammis and Ashby*'s [1986]. The rock of porosity ϕ is idealized as an elastic matrix (with fracture toughness K_{IC}) that contains randomly distributed spherical pores (of radius r). *Zhu et al.* [2010] have developed an analytic approximation for the UCS predicted by this pore-emanated cracking model of *Sammis and Ashby* [1986]:

$$\mathrm{UCS} = \frac{1.325}{\phi^{0.414}} \frac{K_{IC}}{\sqrt{\pi r}} \tag{1}$$

Since our microstructural observations in failed samples of Leitha limestone (Figures 12a and 12b) indicate extensive pore-emanating microcracking, we compare in Figure 14a our UCS data with the analytic prediction (1) of the micromechanical model, assuming for K_{IC} the value of 0.2 MPa.m$^{1/2}$ determined experimentally for calcite by *Atkinson and Meredith* [1987]. Pore radius so inferred from the damage mechanics model increases from 40 μm to 235 μm, corresponding to porosity increase from 18% to 31%. The agreement between data and model is reasonable, in the sense that the inferred diameters (80 μm to 470 μm) coincide with values for macropores we derived from morphological analysis of μCT data (Figure 4). A similar conclusion was arrived at by *Zhu et al.* [2010] for several other limestones.

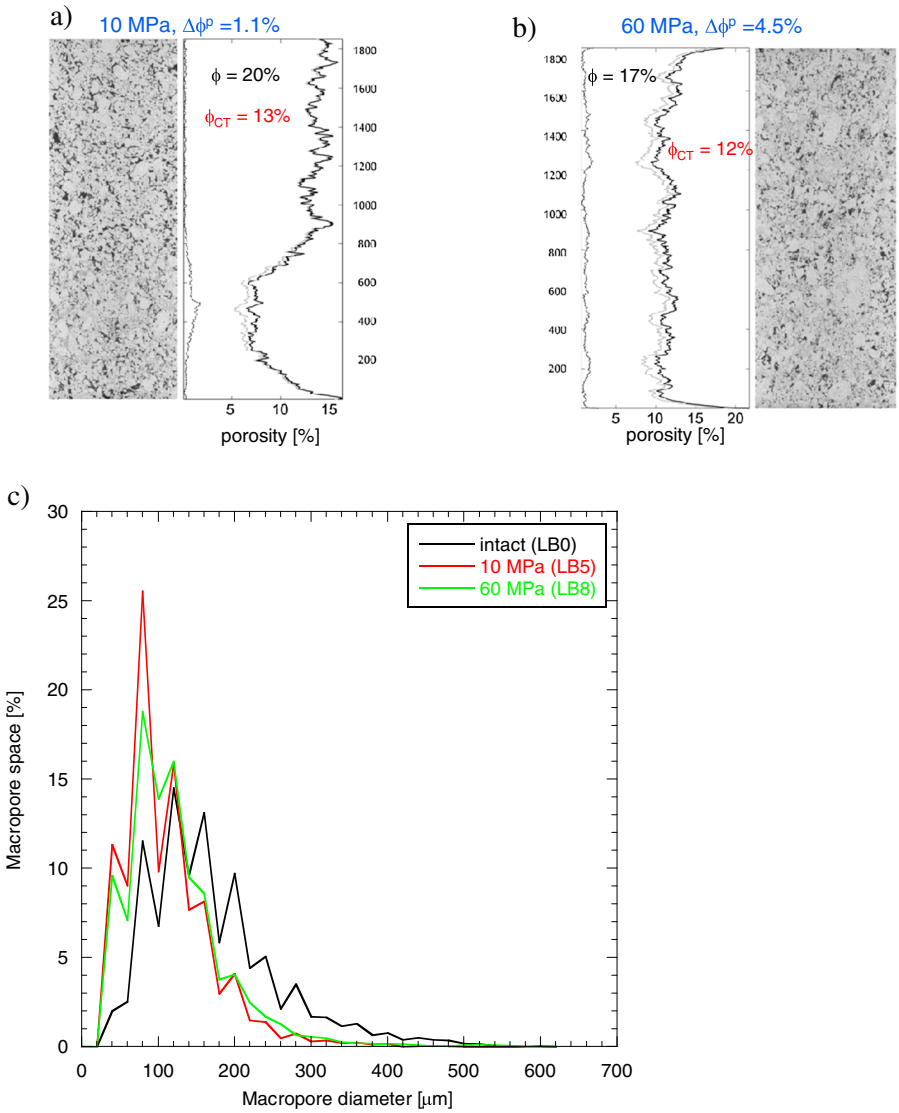

Figure 10. μCT data on samples of Leitha limestone of initial porosity 21% deformed at (a) 10 MPa and (b) 60 MPa of effective pressures. Direction of σ_1 is vertical. Strain localization is at P_{eff} = 10 MPa. Statistics on total, connected, and unconnected porosity are also presented. The porosity of samples inferred from the μCT images and inferred from mechanical data is given in black and red in the figures, respectively. (c) Macropore distribution in intact sample (black) and samples deformed at P_{eff} = 10 MPa (red) and P_{eff} = 60 MPa (green). Macropore space is presented as a function of macropore diameter.

However, because the micromechanical model idealizes the pores as spheres of uniform size, a more definitive comparison with the behavior in a rock with polydisperse pores is difficult. For the most compact sample (18% porosity), the inferred diameter of 80 μm is somewhat smaller than the mean, whereas for the most porous sample (31% porosity) the inferred diameter of 470 μm is at the high end. The apparent discrepancy may be due to the limitation of the model to realistically capture the complex interaction and coalescence of a collection of polydisperse pores, the contributions of which toward failure may not be identical.

Beyond uniaxial compression, our triaxial compression data for the less porous samples show a very narrow range of confinement that falls in the brittle regime, with brittle faulting but negligible dilatancy. For the more porous samples brittle faulting was not observed at all. This is in overall agreement with previous data on high-porosity limestones [*Baud et al.*, 2009]. We also observed that variability in the results tends to increase significantly for more porous samples (31% porosity), as shown in Figure 8. Our μCT data suggest random presence of very large pores, which would tend to make some samples significantly weaker and contribute to this variability.

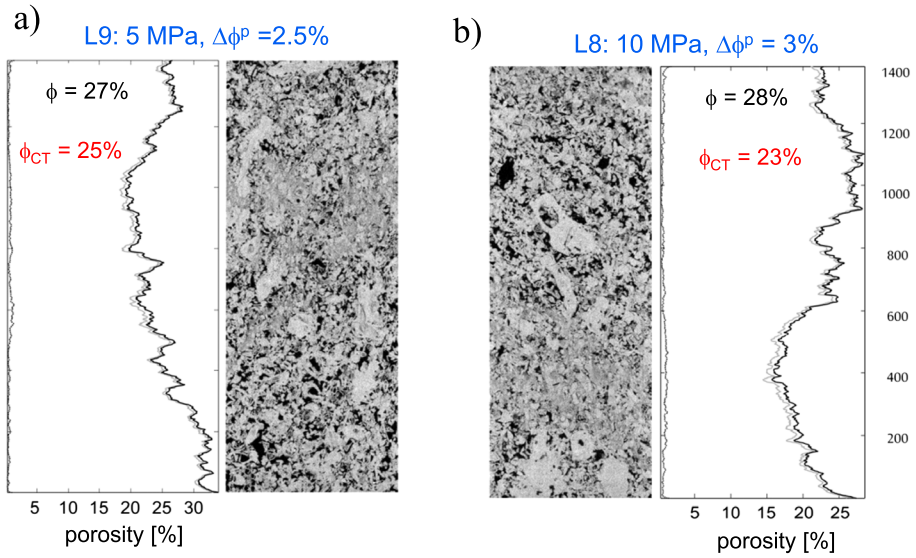

Figure 11. μCT data on samples of Leitha limestone of initial porosity 31% deformed at (a) 5 MPa and (b) 10 MPa of effective pressures. Compaction localization is obvious in both samples. Statistics on total, connected, and unconnected porosity are also presented. The porosity of the samples inferred from the μCT images and inferred from mechanical data are given in black and red in the figures, respectively. Direction of σ_1 is vertical.

7.2. Micromechanics of Inelastic Compaction

Under high confinement, the onset of pore collapse and shear-enhanced compaction are marked by the critical stresses *P** and *C** (Figure 8). Our μCT and SEM observations (Figures 10–13) have highlighted the evolution of damage induced by inelastic compaction in Leitha limestone samples. The hydrostatically compacted samples have critical pressures *P** that correlate quite well with porosity values, and the data can again be fitted empirically with a quadratic relation (Figure 14b). For comparison we include in the figure published data for dry allochemical limestone and chalk compiled by *Zhu et al.* [2010].

Except for the most compact sample (18% porosity), the overall trend is that for a given porosity, our Leitha limestone value seems consistently higher than that of other allochemical limestones. Noting that some water-weakening effect related to stress corrosion is expected in limestone [*Bergsaker et al.*, 2016] in our saturated samples, the corresponding *P** values for dry Leitha limestone samples may be higher, and therefore, discrepancy with the published data could be more pronounced. In their compilation, *Zhu et al.* [2010] focused on limestones with comparable macroporosity and microporosity, for which they developed the cataclastic pore collapse model to explain the initiation and development of pore collapse in a dual porosity medium. Discrepancy between their compiled data and our new data indicate that their dual-porosity model is likely inapplicable to Leitha limestone, except possibly for the most compact sample, which our μCT and microstructural measurements suggest to have an appreciable proportion of micropores (Figures 3j and 3l).

In the cataclastic pore collapse model, collapse of a macropore is induced by stress concentration in its periphery, which can be idealized as an elastic medium embedded with numerous micropores of uniform radius *a**. For this model the critical pressure for the onset of pore collapse was derived by *Zhu et al.* [2010] to be

$$P^* = \frac{0.883}{\phi^{0.414}} S^* \tag{2a}$$

with

$$S^* = \frac{K_{IC}}{(\phi^*/\phi)^{0.414}\sqrt{\pi a^*}} \tag{2b}$$

For a given total porosity ϕ , weakening effect increases with increasing microporosity ϕ^* and radius *a**. Figure 14b shows the prediction of this model for *S** = 70 MPa that may apply to three limestones with

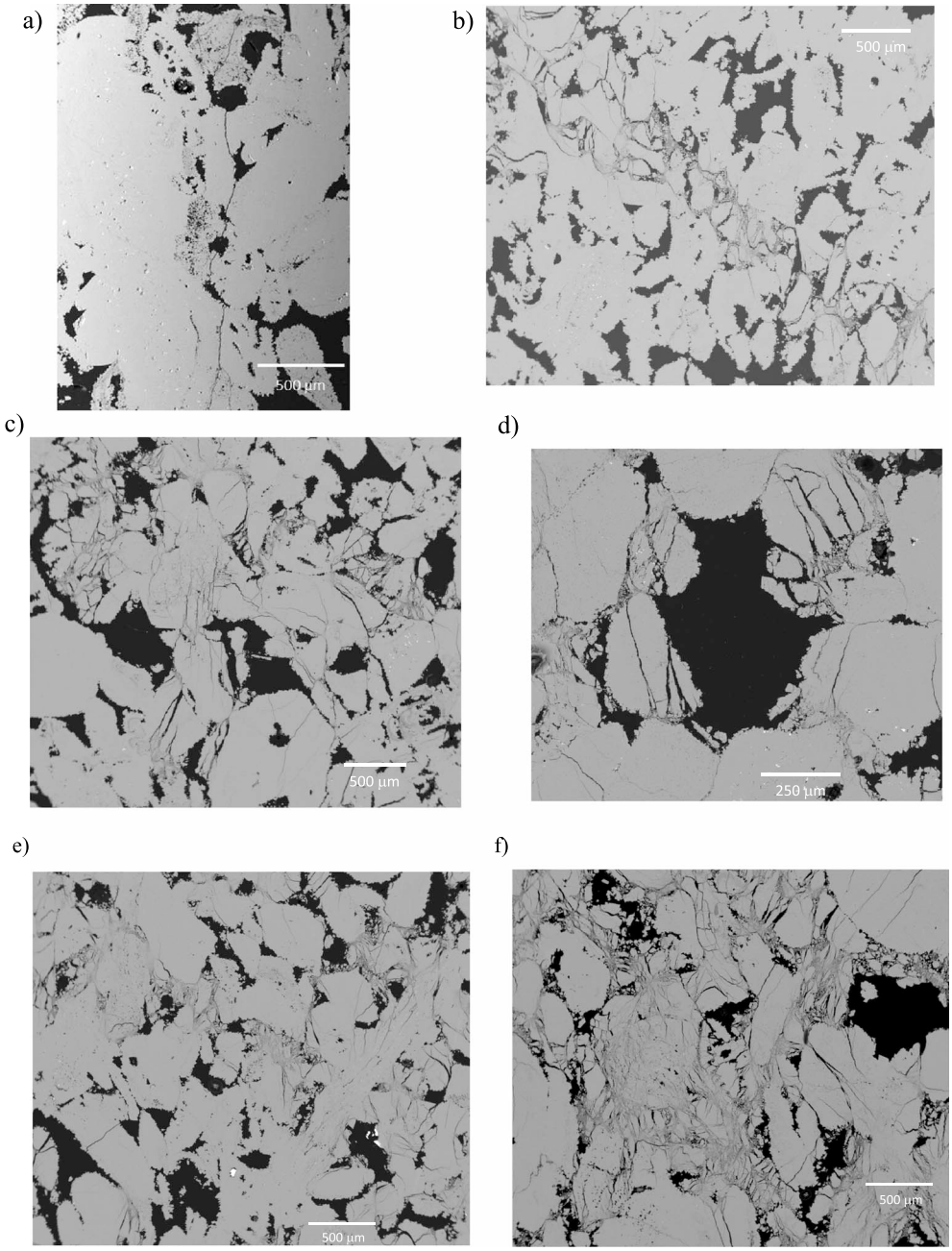

Figure 12. Backscattered images of deformed samples of initial porosity 21%. Direction of σ_1 is vertical. (a) Axial microcracks emanating from macropores in sample L12 deformed uniaxially up to the peak stress. (b) Shear band of about 200 µm thickness in sample LB4 deformed at P_{eff} = 10 MPa beyond the peak stress. (c) Grain crushing and (d) cataclastic pore collapse were observed in conjugated shear bands that developed in sample LB5 deformed at P_{eff} = 20 MPa. Cataclastic flow in samples deformed at 40 MPa of effective pressure. (e) After 5% of axial strain inelastic compaction occurred first in sample LB6 as distributed patches throughout the samples. (f) After 12% of axial strain, higher damage appeared more homogeneously distributed and significantly less macropores were visible in sample LB13.

porosities about 20%, including the most compact Leitha limestone sample (ϕ = 18%). If we again assume a fracture toughness K_{IC} = 0.2 MPa.m$^{1/2}$, then this S^* value would correspond to micropore size of 4 µm, for micropores contributing to 55% of the total porosity (as estimated from the difference between the total porosity and what was resolved by µCT; Figure 3j). The inferred micropore size is consistent with our microstructural observations (Figure 3l).

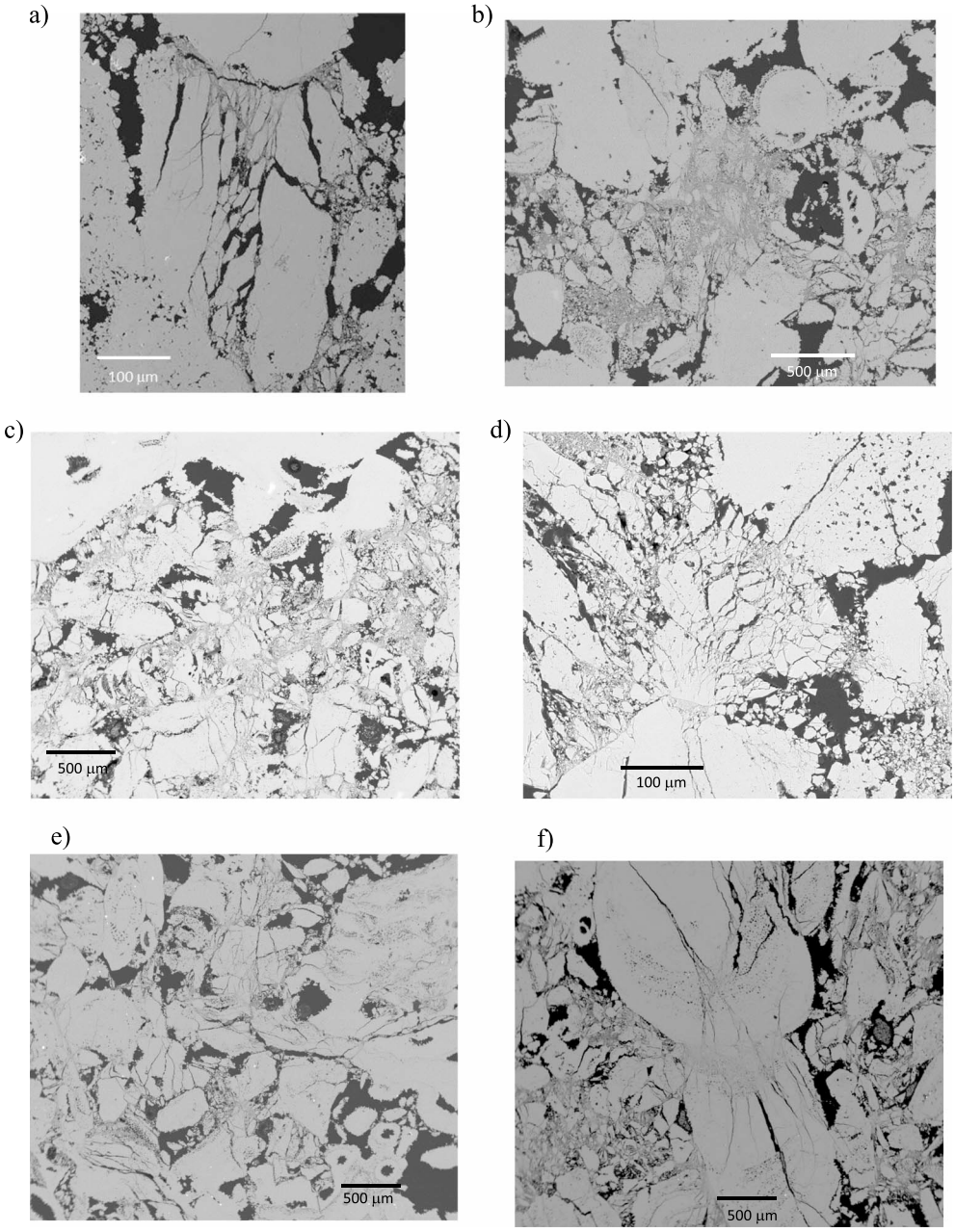

Figure 13. Backscattered images of deformed samples of initial porosity 31%. Direction of σ_1 is vertical. (a) Detail of a compaction band in sample L7 deformed at P_{eff} = 5 MPa. Part of the microcracks initiated at contacts involving grains with low microporosity. (b) Subhorizontal compaction bands in sample L9 deformed at P_{eff} = 5 MPa. The band thickness is 500–700 μm. (c) Another compaction band in sample L8 deformed at P_{eff} = 10 MPa. The bands thickness reached 1.5 mm. (d) Intense grain crushing and pore collapse inside the compaction band. (e) Initiation of cataclastic flow in sample L10 deformed at 20 MPa of effective pressure up to 4% of axial strain. (f) Fracturing of the larger grains in sample L20 deformed at the same effective pressure to 14% of axial strain.

The pore space in the samples with porosities between 21% and 31% is basically made up of primary porosity slightly modified by cementation. In these samples, contacts between bioclasts are relatively well defined and have not been significantly modified either by infilling of cement or production of secondary porosity during diagenesis. The geometric configuration of the impinging bioclast contacts is such that if the sample were subjected to a global stress, the local stress field can be approximated by that of Hertzian contact. If the tensile stress concentration so induced is sufficiently high, microcracks would initiate and emanate

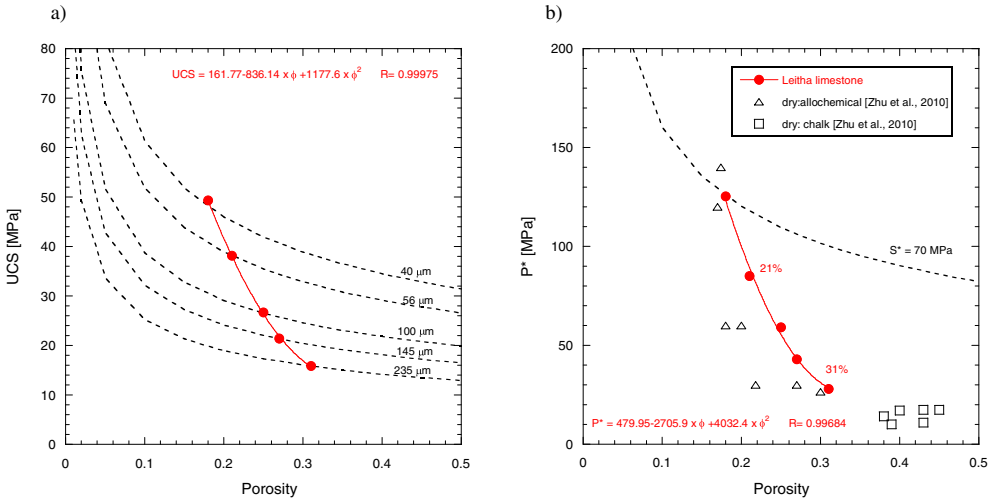

Figure 14. (a) UCS of Leitha limestone as function of porosity. A polynomial fit of the data is presented in red. Theoretical predictions based on the pore-crack model of *Sammis and Ashby* [1986] are presented as dashed lines for different values of the pore radius *r* (equation (1)). (b) Onset of pore-collapse *P** as a function of porosity for samples of Leitha limestone deformed hydrostatically (red circles). Theoretical predictions based on the cataclastic pore-collapse model of *Zhu et al.* [2010] are presented as dashed line for *S** = 70 MPa (equation (2b)). Published dry data on allochemical limestones (open triangles) and chalk (open squares) compiled by *Zhu et al.* [2010] are also shown for reference.

from the contacts, ultimately leading to crushing of the bioclasts and pore collapse. According to the Hertzian fracture model of *Zhang et al.* [1990], the critical pressure for the onset of pore collapse is related to the porosity ϕ and grain radius *R* as follows:

$$P^* = 2.2\left(\frac{1-\nu^2}{E}\right)^2\left(\frac{K_{IC}}{(1-2\nu)}\right)^3(\phi R)^{(-3/2)} \tag{3}$$

Here *E* is the Young modulus and *v* is Poisson's ratio. While *Wong et al.* [1997] showed a good agreement between this model and data on sandstone and sand of a wide range of porosities and grain sizes (Figure 15), *Baud et al.* [2009] found some major discrepancies between the predictions of (3) and data for several porous limestones. Given our microstructural observations, we decided to neglect the relatively small grain sizes of the sparite cement and to simply focus on the bioclasts, and used their average sizes (180–240 μm) as representative values for *R*. It can be seen from Figure 15 that our new *P** data fall on the overall trend defined by sandstone and sand, which implies that inelastic compaction in Leitha limestone likely involves a micromechanical process related to Hertzian fracturing, very similar to that in porous clastic materials.

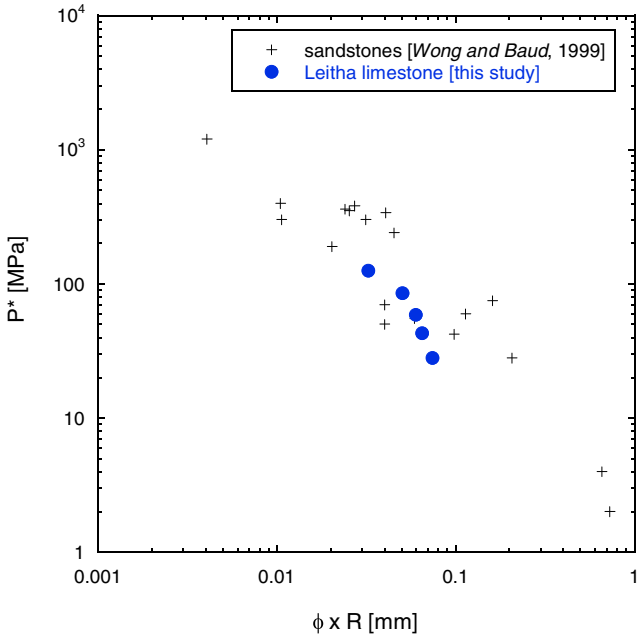

Figure 15. Onset of pore-collapse *P** as a function of the product grain radius × porosity for Leitha limestone (blue circles) and silicilastic rocks (crosses) compiled by *Wong and Baud* [1999].

7.3. Compaction Localization in Porous Carbonates

Our microstructural analysis and μCT data revealed the development of

compaction bands in the most porous samples of Leitha limestone. This failure mode has been studied extensively in porous sandstone for more than a decade. Both field [*Mollema and Antonellini*, 1996; *Schultz et al*., 2010; *Eichhubl et al*., 2010], laboratory [*Baud et al*., 2004; *Tembe et al*., 2008], and theoretical [*Wang et al*., 2008] studies suggest that compaction bands developed in relatively homogeneous high porosity (typically >20%) sandstone. Significantly less work was dedicated to the occurrence of compaction bands in limestone formations, even if several field examples were reported in Italy [*Tondi et al*., 2006; *Rustichelli et al*., 2012] and more recently in Cyprus [*Rotevatn et al*., 2016]. *Rotevatn et al*. [2016] in their recent work only found compaction bands in a rather limited area around an active fault and concluded that these structures could only grow in zones with different and specific host rock properties. Existing laboratory studies support this idea. If a few recent studies reported the development of compaction localization in high-porosity carbonate grainstones such as Orfento and Bolognano formations of Majella [*Cilona et al*., 2012, 2014], Gravina calcarenite [*Arroyo et al*., 2005], or Tuffeau calcarenite of Maastricht [*Baxevanis et al*., 2006], the large majority of limestones studied in the laboratory failed by cataclastic flow in the compactant regime [*Baud et al*., 2000; *Vajdova et al*., 2010, 2012]. Reasons why compaction bands would develop in some carbonates and not in others remain unclear, particularly because some studies on comparable rocks showed contrasted results: *Cilona et al*. [2012] observed, for example, compaction bands in deformed samples of Orfento limestone (Majella mountain Italy), while *Ji et al*. [2015] mapped out the brittle-ductile transition on samples from the same formation (taken from the same quarry) using X-ray μCT and digital image correlation and did not see any compaction band. This again suggests that rather subtle changes in the host rock properties are likely to promote or inhibit the formation of compaction bands in limestone.

Taken together, previous studies and our new results on Leitha limestone suggest that cementation could in fact be the key parameter controlling the development of compaction localization in porous carbonates. Indeed, the 21% and 31% porosity Leitha are very similar rocks, with same composition, very similar grain size and macropore size distributions. The only differences are the degree of cementation and the porosity, parameters obviously not independent one from another. Since the MCIP data, the average particle size and the permeability are almost equal in 21% and 31% porosity Leitha, we can estimate from our CT data and porosity measurements (Figures 3b and 3f) that there is in volume between 5 and 10% more cement in the 21% porosity Leitha, with about 5% filling the intragranular micropores. From our results, we can speculate that increasing cementation inhibit the development of compaction bands in limestone and therefore could explain some of the discrepancies between previous studies described earlier. In sandstone, a compaction band could be seen as a cascade of grain crushing events that can occur suborthogonal to the major principal stress preferentially when the grain size distribution is relatively homogeneous. If this is not the case, larger grains can stop the band propagation and damage can start somewhere else in the rock [*Cheung et al*., 2012]. Our μCT data suggest that cementation in Leitha limestone somehow played a comparable role than that of grain size distribution in sandstone. In the 31% porosity Leitha, intragranular porosity makes the grains weaker, and this combined with minimal cementation creates a relatively homogeneous structure in terms of strength. If damage starts somewhere in the rock, it is plausible that stress redistribution would promote the lateral progression of damage, similar to what was shown in the DEM simulations of *Wang et al*. [2008]. Preexisting heterogeneities such as bedding would also promote the development of such compaction bands, in agreement with recent results of *Cilona et al*. [2014]. In contrast, with more cementation as in the 21% porosity Leitha, grains are significantly stronger and increasing cement creates some stronger (more cemented) areas in the rock (see Figures 3e–3f). Grain crushing would in that case start again where stress concentrations are higher but strong non porous grains will stop damage propagation, and damage would start somewhere else, leading to cataclastic flow. Numerical simulations should be performed to confirm our conclusions.

7.4. Porosity-Permeability Relation in Leitha Limestone

Our measurements of the transport properties (Table S1) indicate an overall trend for permeability to decrease and formation factor to increase with a decrease in porosity. If these changes in transport properties derive primarily from pore size change (with negligible change in pore space connectivity), then the equivalent channel model [*Paterson*, 1983; *Walsh and Brace*, 1984] can effectively characterize geometric attributes of the pore space. This model predicts that the mean hydraulic radius m is related to the permeability k and formation factor F as follows:

$$m = \sqrt{bkF} \tag{4}$$

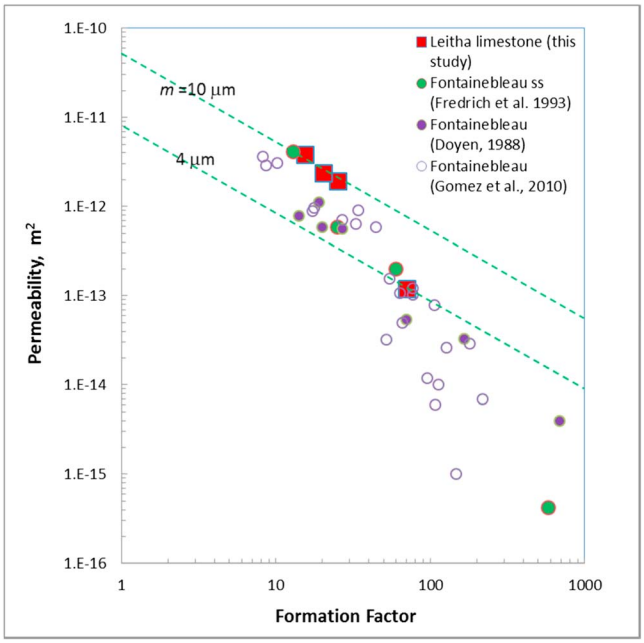

Figure 16. Permeability as a function of formation factor for Leitha limestone (red squares) and published data on Fontainebleau sandstone from *Fredrich et al.* [1993] (green solid circles), *Doyen* [1988] (purple solid circles), and *Gomez et al.* [2010] (purple open circles). The prediction of the equivalent channel model are presented as green dashed like for hydraulic radius *m* of 4 and 10 μm.

Here *b* is a geometric factor, with values of 2 and 3 for circular tubes or cracks, respectively. For constant hydraulic radius and geometric factor, the equivalent channel model predicts that the permeability and reciprocal of formation factor are linearly related. We plot in Figure 16 the Leitha data for permeability versus formation factor. The three more porous samples fall on a linear trend, which corresponds to (4) with geometric factor $b = 2$ and hydraulic radius $m = 10$ μm (Table S1). In this conceptual model, transport is controlled by "throats" in the form of cylindrical tubes with relatively small hydraulic radius, even though storage may be primarily in "nodal pores" with dimension 1 to 2 orders of magnitude larger, comparable to the macropores imaged by μCT.

According to the equivalent channel model, on the average, the hydraulic radius in Leitha limestone did not undergo much change, even when cementation had reduced the porosity from 31% to 21%. This would imply that cement in these samples mainly accumulated in the vicinity of grain contacts or nodal pores, without significantly impacting the throats that control transport. Microstructural observations (Figures 3g and 3h) also showed that a significant part of the cement filled the micropores with little impact on the macroporous network. However, with further porosity reduction to 18%, the model suggests a qualitative change in the throat dimension, with a drastic decrease to a hydraulic radius $m = 4$ μm (Table S1). SEM observations also indicate a larger proportion of micropores in this sample.

To gain further insights into the influence of cementation on the evolution of transport properties, we compare in Figure 16 laboratory data [*Doyen*, 1988; *Fredrich et al*., 1993; *Gomez et al*., 2010] for Fontainebleau sandstone samples with porosities ranging from 25%. down to 4%, related to increasing quartz cementation. Detailed microstructural observations of *Fredrich et al.* [1993] confirmed a progressive decrease of the throat dimension from 10 μm to 6 μm in three samples (with porosities of 20.5%, 15.9%, and 10.7%), which is comparable to a decrease of the hydraulic radius from 10 μm to 4 μm as inferred from (4) for Leitha limestone (corresponding to porosity decrease from 21.6% to 18.5%). However, in the highly cemented sample of Fontainebleau sandstone with 4.1% porosity, significant discrepancy between measurement and equivalent channel model was observed. Whereas high-resolution measurement using laser confocal microscopy indicated pore dimension to have stabilized and not decreased further in this most compact sample, using (4) would predict *m* to decrease drastically to 0.7 μm. The discrepancy is attributed to the failure of the equivalent channel model to realistically capture connectivity changes in the pore space [*Fredrich et al*., 1993]. If indeed the Leitha limestone had undergone more extensive cementation, then the behavior in Fontainebleau sandstone would provide a proxy for corresponding changes in the transport properties.

Since we also performed mercury injection capillary pressure analysis, the MICP data can be used to probe the pore geometry further. Based on their analysis of percolation in a porous medium, *Katz and Thompson* [1987] proposed the following relation between permeability and formation factor:

$$k = \frac{1}{226}(l_c)^2 F^{-1} \tag{5}$$

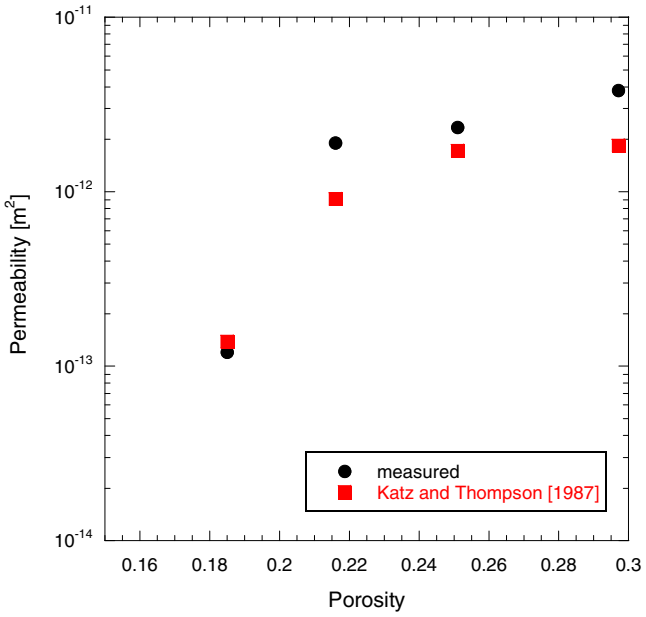

Figure 17. Permeability as a function of porosity for Leitha limestone (black circles) and predictions of *Katz and Thompson* [1987] model (red squares) based on the mercury injection data of Figure 4d.

where l_c is the critical diameter of the throat that allows percolation through the sample, which one can infer from the inflection point in the MICP curve. Increasing pressure beyond this inflection point would progressively push fluid into some of the smaller throats. *Katz and Thompson* [1987] obtained data for Austin chalk and more than 10 sandstones (with porosities ranging from 4% to 35%), which showed very good agreement with their model prediction (5). Nevertheless, application of this percolation model to carbonate rocks can be ambiguous, since many have dual porosity associated with two inflection points in their curves. However, the MICP data of each of our Leitha limestone samples show only one inflection point l_c, which can therefore be used in (5) to uniquely infer permeability from formation factor. The values of l_c we inferred from MCIP (Table S1) are larger than the average hydraulic radii inferred from (4), and near the lower end of the macropore size (Figure 4). It can be seen from Figure 17 that our experimental measurements of permeability are in good agreement with prediction of *Katz and Thompson* [1987] model. Related to the effect of cementation and other diagenetic processes, it is of interest to note that *Milsch et al*. [2008] obtained data for a Fontainebleau sandstone sample with 7.5% porosity. Using their measured formation factor of 121.1 and critical diameter value of 19.77 μm inferred from MICP, the percolation model (5) would predict a permeability of 1.4×10^{-14} m^2, in reasonable agreement with their measured value of 2.2×10^{-14} m^2. In contrast, for 14 oolitic limestone samples with pore space dominated by microporosity, *Casteleyn et al*. [2011] recently concluded that the *Katz and Thompson* [1987] model would not be applicable, since it consistently underestimates the permeability by about one order of magnitude.

8. Conclusions

On the basis of our systematic investigation of mechanical failure, strain localization, and permeability in Leitha limestone using rock mechanics testing, X-ray μCT imaging, and microstructural observations, we have arrived at a number of conclusions.

1. Sampling of rocks from the same formation over a large interval of porosity, we obtained a very clear and simple relation between porosity and mechanical strength in both the brittle and ductile regimes. Larger porosity in Leitha limestone resulted in a spectacular decrease of its strength in both regimes. The simple quadratic relations porosity-strength based on our new data could potentially be used as guidance in field scale problems related to reservoirs/aquifers or geotechnical applications involving porous carbonates.
2. While micromechanical modeling confirmed that the micromechanism leading to brittle failure of a porous limestone is pore-emanated cracking, the main micromechanism of inelastic compaction in Leitha limestone is grain crushing, in contrast with other limestones with a dual porosity.
3. Compaction bands were observed in the less cemented samples of Leitha limestone (31% porosity) but not in more cemented ones (of 21% porosity). Our μCT and mechanical data suggest that increasing cementation created a more heterogeneous structure, in which compaction localization could not develop extensively. Based on our microstructural observations, it is possible that subtle changes in cementation could explain why compaction bands were or were not reported in previous field and laboratory studies, sometimes performed on comparable rocks. More work should be done in particular on field samples to confirm this conclusion.

4. Finally, we found that porosity differences did not have significant influence on the permeability of Leitha limestone, in contrast to mechanical strength. Our μCT data showed that this is essentially due to the existence of a backbone of connected large macropores in all our samples. This also explains the exceptionally high permeability (in the range of 2–5 darcies) of Leitha in comparison to other limestones with similar porosities. In fact, both permeability and formation factor of Leitha are very similar to published data on Fontainebleau sandstone of comparable porosity. An outstanding question for future work would be to which extend mechanical and/or chemical compaction could significantly impact such high permeability.

Acknowledgments
Data will be available on demand. This study was partially funded by the Austrian Science Fund (FWF Project V151-N22), the University of Vienna (Doctoral School IK052), the OeAD Amadeus Project FR 05/201, France-Hong-Kong Collaborative Program Procore 30805PM and F-CUHK405/16, and the Hong Kong Research Grants Council GRF14323916. We thank two anonymous reviewers and the Associate Editor for thoughtful reviews. We are grateful to Bertrand Renaudié who prepared the samples in Strasbourg. We have benefited from discussions with Jamie Farquharson, Yves Guéguen, Michael Heap, and Yuntao Ji.

References

Arroyo, M., R. Castellanza, and R. Nova (2005), Compaction bands and oedometric testing in cemented soils, *Soils Found.*, *45*(2), 181.
Atkinson, B. K., and P. G. Meredith (1987), Experimental fracture mechanics data for rocks and minerals, in *Fracture Mechanics of Rock*, edited by B. K. Atkinson, pp. 477–525, Academic Press, London.
Aydin, A., R. I. Borja, and P. Eichhubl (2006), Geological and mathematical framework for failure modes in granular rock, *J. Struct. Geol.*, *28*(1), 83–98.
Baechle, G. T., A. Colpaert, G. P. Eberli, and R. J. Weger (2008), Effects of microporosity on sonic velocity in carbonate rocks, *Lead. Edge*, 1012–1018.
Baud, P., A. Schubnel, and T.-f. Wong (2000), Dilatancy, compaction, and failure mode in Solnhofen limestone, *J. Geophys. Res.*, *105*, 19,289–19,303, doi:10.1029/2000JB900133.
Baud, P., E. Klein, and T.-f. Wong (2004), Compaction localization in porous sandstones: Spatial evolution of damage and acoustic emission activity, *J. Struct. Geol.*, *26*, 603–624.
Baud, P., V. Vajdova, and T.-F. Wong (2006), Shear-enhanced compaction and strain localization: Inelastic deformation and constitutive modeling of four porous sandstones, *J. Geophys. Res.*, *111*, B12401, doi:10.1029/2005JB004101.
Baud, P., S. Vinciguerra, C. David, A. Cavallo, E. Walker, and T. Reuschlé (2009), Compaction and failure in high porosity carbonates: Mechanical data and microstructural observations, *Pure Appl. Geophys.*, *166*, 869–898.
Baud, P., P. G. Meredith, and E. Townend (2012), Permeability evolution during triaxial compaction of an anisotropic porous sandstone, *J. Geophys. Res.*, *117*, B05203, doi:10.1029/2012JB009176.
Baud, P., T.-f. Wong, and W. Zhu (2014), Effects of porosity and crack density on compressive strength of rocks, *Int. J. Rock Mech. Min. Sci.*, *67*, 202–211.
Baxevanis, T., E. Papamichos, O. Flornes, and I. Larsen (2006), Compaction bands and induced permeability reduction in Tuffeau de Maastricht calcarenite, *Acta Geotech.*, *1*, 123, doi:10.1007/s11440-006-0011-y.
Bednarik, M., B. Moshammer, M. Heinrich, R. Holzer, M. Laho, J. Rabeder, C. Uhlir, and M. Unterwurzacher (2014), Engineering geological properties of Leitha limestone from historical quarries in Burgenland and Styria, Austria, *Eng. Geol.*, *176*, 66–78.
Bemer, E., O. Vincké, and P. Longuemare (2004), Geomechanical log deduced from porosity and mineralogical content, *Oil, Gas Sci. Tech. Rev. IFP*, *59*, 405–426.
Bergsaker, A. S., A. Røyne, A. Ougier-Simonin, J. Aubry, and F. Renard (2016), The effect of fluid composition, salinity and acidity on subcritical crack growth in calcite crystals, *J. Geophys. Res. Solid Earth*, *121*, 1631–1651, doi:10.1002/2015JB012723.
Brantut, N., M. J. Heap, P. Baud, and P. G. Meredith (2014), Mechanisms of time-dependent deformation in porous limestone, *J. Geophys. Res. Solid Earth*, *119*, 5444–5463, doi:10.1002/2014JB011186.
Casteleyn, L., P. Robion, C. David, P.-Y. Collin, B. Menéndez, N. Fernande, G. Desaubliaux, and C. Rigollet (2011), An integrated study of the petrophysical properties of carbonate rocks from the "Oolithe Blanche" formation in the Paris Basin, *Tectonophysics*, *503*, 18–33.
Cheung, C., P. Baud, and T.-f. Wong (2012), Effect of grain size distribution on the development of compaction localization in porous sandstone, *Geophys. Res. Lett.*, *39*, L21302, doi:10.1029/2012GL053739.
Choquette, P. W., and L. C. Pray (1970), Geologic nomenclature and classification of porosity in sedimentary carbonates, *AAPG Bull.*, *54*, 207–250.
Cilona, A., P. Baud, E. Tondi, F. Agosta, S. Vinciguerra, A. Rustichelli, and C. J. Spiers (2012), Deformation bands in porous carbonate grainstones: Field and laboratory observations, *J. Struct. Geol.*, *45*, 137–157.
Cilona, A., D. R. Faulkner, E. Tondi, F. Agosta, L. Mancini, A. Rustichelli, P. Baud, and S. Vinciguerra (2014), The effects of rock heterogeneity on compaction localization in porous carbonates, *J. Struct. Geol.*, *67*, 75–93.
Croizé, D., F. Renard, and J.-P. Gratier (2013), Compaction and porosity reduction in carbonates: A review of observations, theory, and experiments, *Adv. Geophys.*, *54*, 181–238.
Curran, J. H., and M. M. Carroll (1979), Shear stress enhancement of void compaction, *J. Geophys. Res.*, *84*, 1105–1112, doi:10.1029/JB084iB03p01105.
Dautriat, J., N. Gland, A. Dimanov, and J. Raphanel (2011), Hydromechanical behavior of heterogeneous carbonate rock under proportional triaxial loading, *J. Geophys. Res.*, *116*, B01205, doi:10.1029/2009JB000830.
Doyen, P. M. (1988), Permeability, conductivity and pore geometry of sandstone, *J. Geophys. Res.*, *93*(B7), 7729–7740, doi:10.1029/JB093iB07p07729.
Dullo, W. (1983), Fossildiagenese im miozänen Leitha-Kalk der Paratethys von Österreich: Ein Beispiel für Faunenverschiebungen durch Diageneseunterschiede, *Facies*, *8*, 1–112.
Eichhubl, P., J. N. Hooker, and S. E. Laubach (2010), Pure and shear-enhanced compaction bands in Aztec sandstone, *J. Struct. Geol.*, *32*, 1873–1886.
Fredrich, J. T., K. H. Greaves, and J. W. Martin (1993), Pore geometry and transport properties of Fontainebleau sandstone, *Int. J. Rock Mech. Min. Sci.*, *30*(7), 691–697.
Folk, R. L. (1980), *Petrology of Sedimentary Rocks*, Hemphill, Austin.
Fuchs, R., and W. Hamilton (2006), New depositional architecture for an old giant. The Matzen Field, Austria, *AAPG Mem.*, *84*, 205–219.
Gomez, C. T., J. Dvorkin, and T. Vanorio (2010), Laboratory measurements of porosity, permeability, resistivity, and velocity on Fontainebleau sandstones, *Geophysics*, *75*(6), E191–E204.
Griggs, D. T., F. J. Turner, and H. C. Heard (1960), Deformation of rocks at 500° to 800° C, in *Rock Deformation. Memoir, Geol. Soc. Am.*, vol. 79, edited by D. Griggs and J. Handin, pp. 39–104.

Haines, T. J., J. E. Neilson, D. Healy, E. A. H. Michie, and A. C. Aplin (2015), The impact of carbonate texture of the quantification of total porosity by image analysis, *Comput. Geosci.*, *85*, 112–125.
Heap, M. J., P. Baud, T. Reuschlé, and P. G. Meredith (2014a), Stylolites in limestones: Barriers to fluid flow?, *Geology*, *42*(1), 51–54.
Heap, M. J., Y. Lavallée, L. Petrakova, P. Baud, T. Reuschlé, N. R. Varley, and D. B. Dingwell (2014b), Microstructural controls on the physical and mechanical properties of edifice-forming andesites at Volcán de Colima, Mexico, *J. Geophys. Res. Solid Earth*, *119*, 2925–2963, doi:10.1002/2013JB010521.
Ji, Y., P. Baud, V. Vajdova, and T.-f. Wong (2012), Characterization of pore geometry of Indiana limestone in relation to mechanical compaction, *Oil Gas Sci. Technol. Rev l'Institut Français du Pétrol.*, doi:10.2516/ogst/2012051.
Ji, Y., S. Hall, P. Baud, and T.-f. Wong (2015), Characterization of pore structure and strain localization in Majella limestone by X-ray computed tomography and digital image correlation, *Geophys. J. Int.*, *200*, 701–719.
Katz, A. J., and A. H. Thompson (1987), Prediction of rock electrical conductivity from mercury injection measurements, *J. Geophys. Res.*, *92*, 699–607, doi:10.1029/JB092iB01p00599.
Kreutzer, N. (1978), The geology of the Lithothamnia horizons of the Badenian (Miocene) in the Matzen oilfield (Vienna Basin), *Erdoel-Erdgas-Z.*, *94*, 129–145.
Lucia, F. J. (1995), Rock-fabric/petrophysical classification of carbonate pore space for reservoir characterization, *AAPG Bull.*, *79*, 1275–1300.
Milsch, H., G. Blöcher, and S. Engelmann (2008), The relationship between hydraulic and electrical transport properties in sandstones: An experimental evaluation of several scaling models, *Earth Planet. Sci. Lett.*, *275*, 355–363.
Mollema, P. N., and M. A. Antonellini (1996), Compaction bands: A structural analog for anti-mode I cracks in aeolian sandstone, *Tectonophysics*, *267*, 209–228.
Nicolas, A., J. Fortin, J.-B. Regnet, A. Dimanov, and Y. Guéguen (2016), Brittle and semi-brittle behaviours of carbonate rock: Influence of water and temperature, *Geophys. J. Int.*, *206*, 438–456.
Paterson, M. S. (1983), The equivalent channel model for permeability and resistivity in fluid-saturated rock: A re-appraisal, *Mech. Mater.*, *2*, 345–352.
Piller, W. E., et al. (2004), Die stratigraphische Tabelle von Österreich 2004 (sedimentäre Schichtfolgen), in *Kommission für die paläontologische und stratigraphische Erforschung Österreichs*, *Österreichische Akademie der Wissenschaften und Österreichische Stratigraphische Kommission*, Wien. [https://geologie.univie.ac.at/fileadmin/user_upload/dep_geodyn_sedim/Wagreich/piller_et_al_2004.pdf.]
Pittman, E. D. (1971), Microporosity in carbonate rocks, *AAPG Bull.*, *55*, 1873–1878.
Rashid, F., P. W. J. Glover, P. Lorinczi, R. Collier, and J. Lawrence (2015), Porosity and permeability of tight carbonate reservoir rocks in the north of Iraq, *J. Pet. Sci. Eng.*, *133*, 147–161.
Rath, A., U. Exner, C. Tschegg, B. Grasemann, R. Laner, and E. Draganits (2011), Diagenetic control of deformation mechanisms in deformation bands in a carbonate grainstone, *AAPG Bull.*, *95*, 1369–1381.
Regnet, J. B., C. David, J. Fortin, P. Robion, Y. Makhloufi, and P. Y. Collin (2015), Influence of microporosity distribution on the mechanical behavior of oolithic carbonate rocks, *Geomech. Energy Environ.*, *3*, 11–23.
Rotevatn, A., E. Thorsheim, E. Bastesen, H. S. S. Fossmark, A. Torabi, and G. Saelen (2016), Sequential growth of deformation bands in carbonate grainstones in the hangingwall of an active growth fault: Implications for deformation mechanisms in different tectonic regimes, *J. Struct. Geol.*, *90*, 27–47.
Royden, L. H. (1985), The Vienna Basin: A thin-skinned pull-apart basin, in *Strike-Slip Deformation, Basin Formation, and Sedimentation*, vol. 37, edited by K. T. Biddle and N. Christie-Blick, pp. 319–338, SEPM Special Publ.
Rutter, E. H., and C. T. Glover (2012), The deformation of porous sandstones: Are Byerlee friction and the critical state line equivalent?, *J. Struct. Geol.*, *44*, 129–140.
Rustichelli, A., E. Tondi, F. Agosta, A. Cilona, and M. Giorgioni (2012), Development and distribution of bed-parallel compaction bands and pressure solution seams in the Bolognano Formation carbonates (Majella Mountain, Italy), *J. Struct. Geol.*, *37*, 181–199.
Sammis, C. G., and M. F. Ashby (1986), The failure of brittle porous solids under compressive stress states, *Acta Metall.*, *34*, 511–526.
Sauer, R., P. Seifert, and G. Wessely (1992), Guidebook to excursions in the Vienna Basin and the adjacent Alpine-Carpathian thrustbelt in Austria, *Mitt. Geol. Ges.*, *85*, 1–264.
Schmid, P. H., M. Harzhauser, and A. Kroh (2001), Hypoxic events on a middle Miocene carbonate platform of the central Paratethys (Austria, Badenian, 14 Ma), *Ann. Naturhist. Mus. Wien*, *102A*, 1–50.
Schultz, R. A., C. H. Okubo, and H. Fossen (2010), Porosity and grain size controls on compaction band formation in Jurassic Navajo sandstone, *Geophys. Res. Lett.*, *37*, L22306, doi:10.1029/22010GL044909.
Strauss, P., M. Harzhauser, R. Hinsch, and M. Wagreich (2006), Sequence stratigraphy in a classic pull-apart basin (Neogene, Vienna Basin). A 3D seismic based integrated approach, *Geol. Carpath.*, *57*(3), 185–197.
Tarokh, A., Y. Li, and J. F. Labuz (2016), Hardening in porous chalk from precompaction, *Acta Geotech.*, 1–5, doi:10.1007/s11440-016-0501-5.
Tembe, S., P. Baud, and T.-f. Wong (2008), Stress conditions for the propagation of discrete compaction bands in porous sandstone, *J. Geophys. Res.*, *113*, B09409, doi:10.1029/2007JB005439.
Tondi, E. (2007), Nucleation, development and petrophysical properties of faults in carbonate grainstones: Evidence from the San Vito Lo Capo peninsula (Sicily, Italy), *J. Struct. Geol.*, *29*, 614–628.
Tondi, E., M. A. Antonellini, A. Aydin, L. Marchegiani, and G. Cello (2006), The role of deformation bands, stylolites and sheared stylolites in fault development in carbonate grainstones of Majella Mountain, Italy, *J. Struct. Geol.*, *28*, 376–391.
Tondi, E., A. Rustichelli, A. Cilona, F. Balsamo, F. Storti, G. Napoli, F. Agosta, P. Renda, and M. Giorgioni (2016), Hydraulic properties of fault zones in porous carbonates, examples from central and southern Italy, *Ital. J. Geosci.*, *135*(1), 68–79.
Tucker, M. E., and V. P. Wright (1991), *Carbonate Sedimentology*, Blackwell, Oxford.
Turner, F. J., D. T. Griggs, and H. C. Heard (1954), Experimental deformation of calcite crystals, *Geol. Soc. Am. Bull.*, *65*, 883–954.
Vajdova, V., P. Baud, and T.-f. Wong (2004), Compaction, dilatancy, and failure in porous carbonate rocks, *J. Geophys. Res.*, *109*, B05204, doi:10.1029/2003JB002508.
Vajdova, V., W. Zhu, T.-M. N. Chen, and T.-f. Wong (2010), Micromechanics of brittle faulting and cataclastic flow in Tavel limestone, *J. Struct. Geol.*, *32*, 1158–1169.
Vajdova, V., P. Baud, L. Wu, and T.-f. Wong (2012), Micromechanics of inelastic compaction in two allochemical limestones, *J. Struct. Geol.*, *43*, 100–117.
Vincent, B., M. Fleury, Y. Santerre, and B. Brigaud (2011), NMR relaxation of neritic carbonates: An integrated petrophysical and petrographical approach, *J. Appl. Geophys.*, *74*, 38–58.
Voorn, M., U. Exner, and A. Rath (2013), Multiscale Hessian fracture filtering for the enhancement and segmentation of narrow fractures in 3D image data, *Comput. Geosci.*, *57*, 44–53.

Wang, B., Y. Chen, and T.-F. Wong (2008), A discrete element model for the development of compaction localization in granular rock, *J. Geophys. Res.*, *113*, B03202, doi:10.1029/02006JB004501.
Walsh, J. B., and W. F. Brace (1984), The effect of pressure on porosity and the transport properties of rock, *J. Geophys. Res.*, *89*(B11), 9425–9431, doi:10.1029/JB089iB11p09425.
Waxman, M. H., and L. J. M. Smits (1968), Electrical conductivities in oil-bearing shaly sand, *Soc. Petrol. Eng. J.*, *8*, 107–122.
Wei, X., M. Duc, M. Hattab, T. Reuschlé, S. Taibi, and J. M. Fleureau (2016), Effect of decompression and suction on macroscopic and microscopic behavior of a clay rock, *Acta Geotech.*, doi:10.1007/s11440-016-0454-8.
Wiedl, T., M. Harzhauser, A. Kroh, S. Coric, and W. E. Piller (2014), From biologically to hydrodynamically controlled carbonate production by tectonically induced paleogeographic rearrangement (middle Miocene, Pannonian Basin), *Facies*, *60*, 865, doi:10.1007/s10347-014-0408-2.
Wong, T.-F., C. David, and W. Zhu (1997), The transition from brittle faulting to cataclastic flow in porous sandstone: Mechanical deformation, *J. Geophys. Res.*, *102*, 3009–3025, doi:10.1029/96JB03281.
Wong, T.-F., and P. Baud (1999), Mechanical compaction of porous sandstone, *Oil Gas Sci. Technol. Rev. l'Institut Français du Pétrol.*, *54*, 715–727.
Wong, T.-F., and P. Baud (2012), The brittle-ductile transition in porous rock: A review, *J. Struct. Geol.*, *44*, 25–53.
Wu, X., P. Baud, and T.-f. Wong (2000), Micromechanics of brittle faulting and cataclastic flow in Darley Dale sandstone, *Int. J. Rock Mech. Min. Sci.*, *37*, 143–160.
Zambrano, M., E. Tondi, L. Mancini, F. Arzilli, G. Lanzafame, M. Materazzi, and S. Torrieri (2017), 3D pore-network quantitative analysis in deformed carbonate grainstones, *Mar. Petrol. Geol.*, *82*, 251–264.
Zhang, J., T.-f. Wong, and D. M. Davis (1990), Micromechanics of pressure-induced grain crushing in porous rock, *J. Geophys. Res.*, *95*, 341–352, doi:10.1029/JB095iB01p00341.
Zhu, W., and T.-F. Wong (1997), The transition from brittle faulting to cataclastic flow: Permeability evolution, *J. Geophys. Res.*, *102*, 3027–3041, doi:10.1029/96JB03282.
Zhu, W., P. Baud, and T.-f. Wong (2010), Micromechanics of cataclastic pore collapse in limestone, *J. Geophys. Res.*, *115*, B04405, doi:10.1029/2009JB006610.
Zinszner, B., and F.-M. Pellerin (2007), *A Geoscientist's Guide to Petrophysics*, Technip, Paris.